JM PAPERS

Diffusion-driven flows in a nonlinear stratified fluid layer

Lingyun Ding†

Department of Mathematics, University of California Los Angeles, CA 90095, USA

Diffusion-driven flow is a boundary layer flow arising from the interplay of gravity and diffusion in density-stratified fluids when a gravitational field is non-parallel to an impermeable solid boundary. This study investigates diffusion-driven flow within a nonlinearly density-stratified fluid confined between two tilted parallel walls. We introduce an asymptotic expansion inspired by the centre manifold theory, where quantities are expanded in terms of derivatives of the cross-sectional averaged stratified scalar (such as salinity or temperature). This technique provides accurate approximations for velocity, density and pressure fields. Furthermore, we derive an evolution equation describing the cross-sectional averaged stratified scalar. This equation takes the form of the traditional diffusion equation but replaces the constant diffusion coefficient with a positive-definite function dependent on the solution's derivative. Numerical simulations validate the accuracy of our approximations. Our investigation of the effective equation reveals that the density profile depends on a non-dimensional parameter denoted as γ representing the flow strength. In the large γ limit, the system is approximated by a diffusion process with an augmented diffusion coefficient of $1 + \cot^2\theta$, where θ signifies the inclination angle of the channel domain. This parameter regime is where diffusion-driven flow exhibits its strongest mixing ability. Conversely, in the small γ regime, the density field behaves like pure diffusion with distorted isopycnals. Lastly, we show that the classical thin film equation aligns with the results obtained using the proposed expansion in the small γ regime but fails to accurately describe the dynamics of the density field for large γ.

Key words: dispersion, lubrication theory, stratified flows

1. Introduction

The density of a fluid is influenced by several factors, including temperature, the concentration of solute and pressure profiles. Typically, these factors lead to a non-uniform distribution of density in the fluid. Density stratified fluids are commonly found in various

† Email address for correspondence: dingly@g.ucla.edu

natural environments, such as lakes, oceans, the Earth's atmosphere, making them a subject of great interest in numerous research endeavours (Linden 1979; Cenedese & Adduce 2008; Magnaudet & Mercier 2020; Camassa *et al.* 2022; More & Ardekani 2023). In the context of density-stratified fluids, achieving hydrostatic equilibrium is contingent upon aligning the density gradients with the direction of gravitational force. In scenarios involving impermeable boundaries and the modelling of diffusive stratified scalars, a no-flux boundary condition applies, demanding that the density gradient be orthogonal to the boundary's normal vector. If the boundary's normal vector is perpendicular to the gravitational direction, the no-flux condition prevents the density gradient from aligning with gravity, thus disrupting hydrostatic equilibrium. The disruption of hydrostatic equilibrium results in the emergence of a boundary layer flow, a phenomenon termed diffusion-driven flow in the field of physics (Phillips 1970; Wunsch 1970), or mountain and valley (katabatic or anabatic) winds (Prandtl, Oswatitsch & Wieghardt 1942; Oerlemans & Grisogono 2002) in meteorology.

The phenomenon of diffusion-driven flow has garnered significant attention across various fields. First, in the context of oceanography, the presence of salt in seawater leads to density stratification. The continental shelf has a gentle slope extending from the coast to the deeper waters of the ocean. The sloping boundaries induce a mean upwelling velocity along the boundaries to satisfy the no-flux condition. This upwelling flow plays a crucial role in facilitating the vertical exchange of oceanic properties (see, for example, Phillips 1970; Wunsch 1970; Dell & Pratt 2015; Holmes, de Lavergne & McDougall 2019; Drake, Ferrari & Callies 2020). Second, fluids confined within long, narrow fissures can also exhibit density stratification. This stratification can result from non-uniform concentration distributions of stratified scalars or vertical temperature gradients. For example, Earth's geothermal gradient induces convective flows that lead to significant solute dispersion on geological time scales (Woods & Linz 1992; Shaughnessy & Van Gilder 1995; Heitz, Peacock & Stocker 2005). Third, when a wedge-shaped object is immersed in a stratified fluid, the resulting diffusion-driven flow can propel the object forward (Allshouse, Barad & Peacock 2010; Mercier *et al.* 2014). The flows generated by such immersed wedge-shaped objects have been further investigated in various contexts (Chashechkin & Mitkin 2004; Zagumennyi & Dimitrieva 2016; Chashechkin 2018; Dimitrieva 2019; Levitsky, Dimitrieva & Chashechkin 2019). Fourth, diffusion-driven flow is one of the mechanisms that induce particle attraction and self-assembly in stratified fluids (Camassa *et al.* 2019; Thomas & Camassa 2023). Fifth, it has been demonstrated that this type of flow can be employed to measure the molecular diffusivity of stratified scalars (Allshouse 2010). Sixth, flows induced by the presence of insulating sloping boundaries play an important role in the layer formation in double-diffusive systems (Linden & Weber 1977).

Despite the significant findings in this field, there are two points that have not been adequately addressed in the existing literature. First, most existing theories primarily pertain to linearly stratified fluids, and there is a scarcity of theoretical investigations into diffusion-driven flow in nonlinearly stratified fluids. Nonlinearly stratified fluids are more prevalent in various natural environments, making theoretical analysis in this context highly applicable. Second, there can exist two different type of scalars in the fluid: the stratified scalar and the passive scalar. The stratified scalar causes non-uniform density distributions in the fluid and drives diffusion-driven flow. In contrast, the passive scalar represents the concentration of a different solute (in some cases, the temperature field) that does not contribute to density variation but is instead passively advected by the fluid flow. It is well-established that fluid flow enhances solute mixing in the fluid (Lin,

Thiffeault & Doering 2011; Thiffeault 2012; Aref *et al.* 2017). Many studies focus on how diffusion-driven flow enhances the dispersion of a passive scalar (Woods & Linz 1992; Ding & McLaughlin 2023) and the corresponding analysis for the stratified scalar is rare. Experiments, such as the one documented in Ding (2022), illustrate that the dispersion of the stratified scalar in a tilting capillary pipe exhibits a higher dispersion rate compared with a vertically oriented pipe. This qualitative demonstration highlights the role of diffusion-driven enhancement at microscales. At diffusion time scales, the concentration of a diffusing passive scalar under the advection of shear flows can be described by an effective diffusion equation with an effective diffusion coefficient (Taylor 1953; Aris 1956). Consequently, it is of interest to establish the evolution equation for the concentration of the stratified scalar. This would enable us to quantitatively describe how diffusion-driven flow enhances the spreading rate of the stratified scalar.

To address these research gaps, this paper delves into the study of an incompressible viscous density stratified fluid layer confined between two infinite parallel walls. Investigating this fundamental domain geometry can enhance our comprehension of more intricate shapes found in real-world scenarios, such as rock fissures and capillary pipes. Furthermore, it provides a versatile framework for comprehending fluid dynamics within confined spaces, which holds substantial practical significance.

Our primary objectives are to derive approximations for the velocity field and density field and to determine the equation governing the dynamics of the fluid density field at diffusion time scales. One conventional approach, such as thin film approximation, involves introducing a small parameter and utilizing power series expansions for all relevant quantities with respect to this parameter. However, we demonstrate that results obtained through thin film approximation are only valid within specific parameter ranges and do not provide uniformly accurate approximations across all parameters. To obtain an approximation that accurately describes density dynamics across a wider parameter range, we adopt an alternative expansion method inspired by centre manifold theory (Mercer & Roberts 1990; Roberts 1996; Ding & McLaughlin 2022*a*). In this alternative approach, we assume that the density field varies slowly in the longitudinal direction of the channel. Then all quantities are represented in terms of derivatives of the averaged stratified scalar. This innovative approach enhances our ability to achieve accuracy in a broader range of flow scenarios.

This paper is organized as follows. In § 2, we formulate the governing equations for diffusion-driven flow and outline the procedure for non-dimensionalization. Section 3 introduces an asymptotic expansion technique for the velocity, density and pressure fields. Using this approach, we derive the leading-order approximation for the velocity field and establish the evolution equation for the cross-sectional averaged stratified scalar, referred to as the effective equation in subsequent sections. In § 3.3, we conduct numerical simulations of the full governing equations to demonstrate the validity of the asymptotic approximations. Section 4 delves deeper into the properties of the effective equation, providing a more comprehensive understanding of its behaviour in various scenarios. Section 5 documents the results obtained using the thin film approximation and compares them with the expansion proposed in § 3. Finally, in § 6, we summarize our findings and explore potential avenues for future research.

2. Governing equation and non-dimensionalization

This section summarizes the mathematical formulation of the problem and documents the non-dimensionalization procedure for the governing equation.
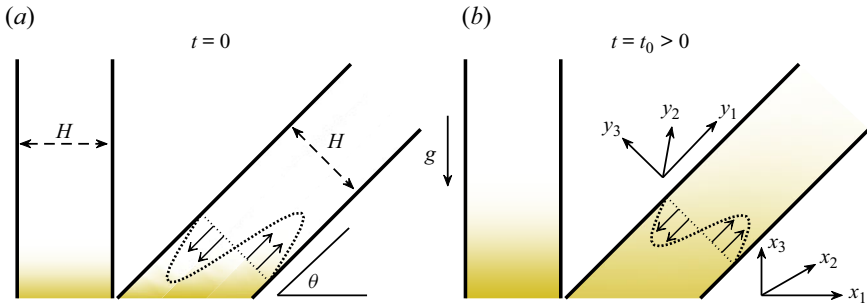
Figure 1. This schematic illustrates the set-up for the diffusion-driven flow problem. Tilted impermeable boundaries induce the diffusion-driven flow, while there is no flow in the vertically oriented channel ($\theta = \pi/2$). Pure molecular diffusion governs the scalar distribution in the latter case. As depicted in (*a*), at $t = 0$, the concentration profiles are approximately the same in both channels. However, as time progresses, the dispersion of the scalar becomes more pronounced in the tilted channel compared with the vertically oriented one. In addition, the flow strength decreases as the density gradient decreases.

2.1. *Governing equation*

Figure 1 sketches two coordinate systems for a tilted parallel-plate channel domain with an inclination angle θ relative to the horizontal plane, which satisfies $0 \le \theta \le \pi/2$. In this set-up, the x_3-direction is parallel to the direction of gravity. Here $\Omega = \{y_3 | y_3 \in [0, H]\}$ is the cross-section of the channel, where H is the distance between plates. The longitudinal direction of the channel is denoted as the y_1-direction, with $y_1 \in [-L, L]$, where L may be either infinite or a finite number that is significantly larger than H. The relation between the laboratory frame coordinates (x_1, x_2, x_3) and the coordinates (y_1, y_2, y_3) is

$$\begin{bmatrix} y_1 \\ y_3 \end{bmatrix} = \begin{bmatrix} \cos\theta & \sin\theta \\ -\sin\theta & \cos\theta \end{bmatrix} \begin{bmatrix} x_1 \\ x_3 \end{bmatrix}, \quad y_2 = x_2. \tag{2.1}$$

In the (y_1, y_2, y_3) coordinate system, gravity acts along the direction $(-\sin\theta, 0, -\cos\theta)$. Experimental methods described in Allshouse (2010) and Heitz *et al.* (2005) provide feasible set-ups for this study. Another promising experimental configuration involves using temperature-stratified liquid gallium (Braunsfurth *et al.* 1997).

We consider a scalar c responsible for fluid density stratification, referred to as the stratified scalar in the subsequent context, such as temperature or solute concentration. The density is assumed to be a specified function of the stratified scalar. For example, Abaid *et al.* (2004) obtained the formula for the density of a sodium chloride solution as $\rho = 0.9971 + 0.00065S + 0.000322(25 - T)$ g cm^{-3}, where salinity S is measured in parts per thousand and temperature T is in degrees Celsius. In cases with a broader range of salinity, the relationship may exhibit nonlinearity. Hall (1924), through empirical data fitting, established $\rho = 0.997071 + 0.00070109S + 1.3268 \times 10^{-7}S^2 + 3.535 \times 10^{-10}S^3$ g cm^{-3} for sodium chloride solutions at 25 °C. The theoretical method presented in this work can be easily extended to cases with variable fluid viscosity. However, for simplicity, we assume the fluid dynamic viscosity is constant throughout the paper.

The stratified scalar c and the fluid flow $\boldsymbol{u} = (u_1, u_2, u_3)$ in the $\boldsymbol{x} = (x_1, x_2, x_3)$ direction satisfy the incompressible Navier–Stokes equation,

$$\left. \begin{array}{l} \rho(c)(\partial_t u_i + \boldsymbol{u} \cdot \nabla u_i) = \mu \Delta u_i - \partial_{x_i} p - \rho(c)g\delta_{i3}, \quad u_i|_{\boldsymbol{x} \in \partial\Omega} = 0, \quad i = 1, 2, 3, \\ \nabla \cdot \boldsymbol{u} = 0, \quad \partial_t c + \boldsymbol{u} \cdot \nabla c = \kappa \Delta c, \quad \partial_{\boldsymbol{n}} c|_{\boldsymbol{x} \in \partial\Omega} = 0, \quad c|_{t=0} = c_I(\boldsymbol{x}), \end{array} \right\} \tag{2.2}$$

where $\boldsymbol{n}$ is the outward normal vector of the boundary, δ_{ij} is the Kronecker delta, g (cm s^{-2}) is the acceleration of gravity, ρ (g cm^{-3}) is the density, μ (g cm^{-1} s^{-1}) is the dynamic viscosity, p (g cm^{-1} s^{-2}) is the pressure and κ (cm^2 s^{-1}) is the molecular diffusivity of the stratified scalar.

It is convenient to consider the problem in the (y_1, y_2, y_3) coordinate system. We denote v_i as the velocity component along the y_i-direction. Since the initial condition and the boundary condition are independent of y_2, (2.2) reduces to a two-dimensional problem

$$
\left.
\begin{aligned}
\rho(\partial_t v_1 + v_1 \partial_{y_1} v_1 + v_3 \partial_{y_3} v_1) &= \mu \Delta v_1 - \partial_{y_1} p - \sin\theta g\rho, \\
\rho(\partial_t v_3 + v_1 \partial_{y_1} v_3 + v_3 \partial_{y_3} v_3) &= \mu \Delta v_3 - \partial_{y_3} p - \cos\theta g\rho, \\
\partial_t c + \boldsymbol{v} \cdot \nabla c = \kappa \Delta c, \quad \nabla \cdot \boldsymbol{v} = 0, \quad \boldsymbol{v}|_{y \in \partial\Omega} = \boldsymbol{0}, \quad & \partial_{\boldsymbol{n}} c|_{y \in \partial\Omega} = 0.
\end{aligned}
\right\}
\tag{2.3}
$$

In this study, we assume the initial density profile is a stable density stratification, where the density decreases monotonically as the height increases, namely, $\partial_{y_1} \rho(\bar{c}_I) \leq 0$. For convenience, we use the overline to represent the cross-sectional average of a quantity and use the tilde to represent the fluctuation, for example, $\overline{c_I}(y_1) = \int_0^1 c_I(y_1, y_3) \, \mathrm{d}y_3$.

2.2. *Non-dimensionalization*

As the flow is driven by molecular diffusion, we select the diffusion time scale as the characteristic time, H^2/κ. Specifically, it refers to the time it takes for solute molecules to diffuse across the cross-sectional area of the channel domain. Utilizing the following change of variables for non-dimensionalization:

$$
\rho_0 \rho' = \rho, \quad c_0 c' = c, \quad \frac{H^2}{\kappa} t' = t, \quad Hy' = y, \quad Uv' = v, \quad \frac{\mu U}{H} p' = p,
\tag{2.4}
$$

then (2.3) becomes

$$
\left.
\begin{aligned}
\rho' \left(\frac{U\kappa}{H^2} \partial_{t'} v_1' + \frac{U^2}{H} v_1' \partial_{y_1'} v_1' + \frac{U^2}{H} v_3' \partial_{y_3'} v_1' \right) &= \frac{\mu U}{H^2 \rho_0} \Delta_{y'} v_1' - \frac{\mu U}{H^2 \rho_0} \partial_{y_1'} p' - \sin\theta g\rho', \\
\rho' \left(\frac{U\kappa}{H^2} \partial_{t'} v_3' + \frac{U^2}{H} v_1' \partial_{y_1'} v_3' + \frac{U^2}{H} v_3' \partial_{y_3'} v_3' \right) &= \frac{\mu U}{H^2 \rho_0} \Delta_{y'} v_3' - \frac{\mu U}{H^2 \rho_0} \partial_{y_3'} p' - \cos\theta g\rho', \\
\frac{c_0 \kappa}{H^2} \partial_{t'} c' + \frac{U c_0}{H} v' \cdot \nabla_{y'} c' &= \frac{\kappa c_0}{H^2} \Delta_{y'} c', \quad \frac{c_0}{H} \partial_{\boldsymbol{n}'} c'|_{y' \in \partial\Omega'} = 0.
\end{aligned}
\right\}
\tag{2.5}
$$

We can drop the primes without confusion and obtain the non-dimensionalized version

$$
\left.
\begin{aligned}
\rho \left(\frac{1}{Sc} \partial_t v_1 + Re v_1 \partial_{y_1} v_1 + Re v_3 \partial_{y_3} v_1 \right) &= \Delta v_1 - \partial_{y_1} p - Re\, Ri\rho \sin\theta, \\
\rho \left(\frac{1}{Sc} \partial_t v_3 + Re v_1 \partial_{y_1} v_3 + Re v_3 \partial_{y_3} v_3 \right) &= \Delta v_3 - \partial_{y_3} p - Re\, Ri\rho \cos\theta, \\
\partial_t c + Pe \boldsymbol{v} \cdot \nabla c &= \Delta c,
\end{aligned}
\right\}
\tag{2.6}
$$

where the non-dimensional parameters are Péclet number $Pe = UH/\kappa$, Reynolds number $Re = \rho_0 HU/\mu$, Richardson number $Ri = gH/U^2$ and Schmidt number $Sc = \mu/\rho_0\kappa = Pe/Re$. If the scalar field is the temperature field, then κ is the thermal diffusivity and $Pr = \mu/\rho_0\kappa = Pe/Re$ is the Prandtl number.

We proceed by examining a combination of experimental physical parameters, which can provide us with the order of magnitude of the non-dimensional parameters and assist

in our perturbation analysis. The previous experiments primarily focused on diffusion in linearly stratified fluids. It is feasible to adapt these set-ups for experiments involving nonlinearly stratified fluids, making the parameters therein useful as reference points. For instance, in Camassa *et al.* (2019), a linear density stratification of the fluid was achieved using sodium chloride. The relevant physical parameters in this context are as follows: $g = 980$ cm s^{-2}, $\mu_0 = 0.008903$ g (cm s)$^{-1}$, $\kappa = 1.5 \times 10^{-5}$ cm^2 s^{-1} (Vitagliano & Lyons 1956), $\rho_0 = 0.9971$ g cm^{-3}, the vertical density gradient $\partial_{x_3}\rho$ is a constant 0.007 g cm^{-4}. The scaling relation for the characteristic velocity and the physical parameters varies depending on the boundary geometries. For a linear stratified fluid, the characteristic velocity and characteristic boundary layer thickness of steady diffusion-driven flow in a parallel-plate channel can be calculated using the formula from (Phillips 1970; Heitz *et al.* 2005) as follows:

$$U = 2\kappa \cot(\theta) \left(\frac{g \sin(\theta)\partial_{x_3}\rho}{4\kappa\mu} \right)^{1/4}, \quad H_b = \left(\frac{g \sin(\theta)\partial_{x_3}\rho}{4\kappa\mu} \right)^{-1/4}. \quad (2.7a,b)$$

Using these formulae, we obtain the values $U = 0.00164684$ cm s^{-1}, $H_b = 0.0182167$ cm for $\theta = \pi/4$. When the gap thickness between two walls is $H = 0.1$ cm, this leads to the following non-dimensional parameters:

$$Re = 0.0184512, \quad Pe = 10.9799, \quad Sc = 595.076, \quad Re\,Ri = 666613. \quad (2.8a{-}d)$$

It is evident that the Reynolds number is small, indicating that viscous effects dominate the flow, and the gravity term is significant in the governing equation.

Last, with the above parameters and $c_0 = 1$ mol kg^{-1}, the relation between ρ and c can be expressed as

$$\rho(c) = 1 + 0.0410921c + 0.000454464c^2 + 0.000070761c^3. \quad (2.9)$$

3. Asymptotic analysis and numerical simulation

In this section, our goal is to derive approximations for the velocity and density fields and validate them through numerical simulations.

The hydrostatic body force terms in the governing equation contribute only to the hydrostatic pressure field. Since they do not influence the velocity and stratified scalar field, we can absorb them into a modified pressure. For convenience, we define $p = p_0 + \tilde{p}$, where

$$\left. \begin{aligned} p_0 &= -Re\,Ri \left(\sin\theta \int_0^{y_1} \rho(\bar{c}(y_1))\,\mathrm{d}y_1 + \cos\theta \left(y_3 - \frac{1}{2} \right) \rho(\bar{c}) \right), \\ \partial_{y_1}p_0 &= -Re\,Ri \left(\sin\theta\rho(\bar{c}) + \cos\theta \left(y_3 - \frac{1}{2} \right) \partial_{y_1}\rho(\bar{c}) \right), \quad \partial_{y_3}p_0 = -Re\,Ri \cos\theta\rho(\bar{c}). \end{aligned} \right\} \tag{3.1}$$

Then the governing equation (2.6) becomes

$$\left. \begin{aligned} \rho &\left(\frac{1}{Sc}\partial_t v_1 + Re v_1\partial_{y_1}v_1 + Re v_3\partial_{y_3}v_1 \right) \\ &= \Delta v_1 - \partial_{y_1}\tilde{p} - Re\,Ri \left(\sin\theta(\rho - \rho(\bar{c})) - \cos\theta \left(y_3 - \frac{1}{2} \right) \partial_{y_1}\rho(\bar{c}) \right), \\ \rho &\left(\frac{1}{Sc}\partial_t v_3 + Re v_1\partial_{y_1}v_3 + Re v_3\partial_{y_3}v_3 \right) = \Delta v_3 - \partial_{y_3}\tilde{p} - Re\,Ri \cos\theta(\rho - \rho(\bar{c})), \\ &\quad\quad \partial_t c + Pe(v_1\partial_{y_1}c + v_3\partial_{y_3}c) = \Delta c, \quad \partial_{y_1}v_1 + \partial_{y_3}v_3 = 0. \end{aligned} \right\} \tag{3.2}$$

3.1. *Expansions for slow varying density profile*

To address the scenario where the longitudinal length scale of the channel domain significantly exceeds the transverse length scale, our objective is to develop a simplified model that relies solely on the longitudinal variable of the channel domain. To achieve this, we adopt the following ansatz for the velocity and density:

$$
\left.
\begin{aligned}
v_1(y_1, y_3, t) &= v_{1,0}(y_3, t, \bar{c}) + v_{1,1}(y_3, t, \partial_{y_1}\bar{c})\partial_{y_1}\bar{c} + v_{1,2}(y_3, t, \partial_{y_1}\bar{c}, \partial_{y_1}^2\bar{c})\partial_{y_1}^2\bar{c} + \cdots, \\
v_3(y_1, y_3, t) &= v_{3,0}(y_3, t, \bar{c}) + v_{3,1}(y_3, t, \partial_{y_1}\bar{c})\partial_{y_1}\bar{c} + v_{3,2}(y_3, t, \partial_{y_1}\bar{c}, \partial_{y_1}^2\bar{c})\partial_{y_1}^2\bar{c} + \cdots, \\
c(y_1, y_3, t) &= \bar{c}(y_1, t) + c_1(y_3, t, \partial_{y_1}\bar{c})\partial_{y_1}\bar{c} + c_2(y_3, t, \partial_{y_1}\bar{c}, \partial_{y_1}^2\bar{c})\partial_{y_1}^2\bar{c} + \cdots, \\
p(y_1, y_3, t) &= p_0(y_1, y_3, t) + p_1(y_3, t, \partial_{y_1}\bar{c})\partial_{y_1}\bar{c} + p_2(y_3, t, \partial_{y_1}\bar{c}, \partial_{y_1}^2\bar{c})\partial_{y_1}^2\bar{c} + \cdots.
\end{aligned}
\right\}
\tag{3.3}
$$

In this expansion, $v_{i,1}, c_1, p_1$ are functions of $\partial_{y_1}\bar{c}$. Here $v_{j,2}, c_2, p_2$ are functions of $\partial_{y_1}\bar{c}$ and $\partial_{y_1}^2\bar{c}$. The jth term in the expansion is contingent on the derivative of $\bar{c}$ up to the jth order. By definition, $\partial_{y_1}\bar{c}$ is independent of y_3 and is solely a function of y_1 and t. For the specific problem we investigate here, both $v_{i,j}$ and c_i are functions of y_3 and t, while their dependence on y_1 is captured through $\partial_{y_1}\bar{c}$. In more general cases, such as the domain with non-flat boundary, $v_{i,j}$ and c_i may depend on y_1.

In our analysis, we consider the derivative of the averaged stratified scalar, $\partial_{y_1}^n\bar{c}$, as a small parameter within the framework of standard asymptotic calculations. Additionally, we assume that higher-order derivatives exhibit smaller magnitudes compared with lower-order derivatives. This assumption is reasonable for systems where diffusion dominates.

To provide an intuitive justification, we assume that flow effects are negligible, and diffusion is the dominant process in the system. Under these conditions, the scalar field exhibits a self-similarity solution represented as $\bar{c} = \frac{1}{2}\mathrm{erfc}(y_1/2\sqrt{t})$, where $\mathrm{erfc}(z) = (2/\sqrt{\pi})\int_z^\infty e^{-t^2}\,dt$. The derivatives of this solution are as follows:

$$
\left.
\begin{aligned}
\partial_{y_1}\bar{c} &= -\frac{e^{-y_1^2/4t}}{2\sqrt{\pi}\sqrt{t}}, \quad \partial_{y_1}^2\bar{c} = -\frac{y_1 e^{-y_1^2/4t}}{4\sqrt{\pi}t^{3/2}}, \\
\partial_{y_1}^n\bar{c} &= -\frac{1}{\sqrt{\pi}}\left(-\frac{1}{2\sqrt{t}}\right)^n H_{n-1}\left(\frac{y_1}{2\sqrt{t}}\right)e^{-(y_1/2\sqrt{t})^2},
\end{aligned}
\right\}
\tag{3.4}
$$

where H_n is the Hermite polynomial of degree n. In general, as t approaches infinity, we have $\partial_{y_1}^n\bar{c} = O(t^{-n+1/2})$. Consequently, as $t \to \infty$, we observe the hierarchy $\bar{c} \gg \partial_{y_1}\bar{c} \gg \partial_{y_1}^2\bar{c} \gg \cdots$. Due to the orthogonality of the Hermite polynomial, $\partial_{y_1}^n\bar{c}$ forms a good basis for approximating the function. In addition, it is important to note that in the presence of a diffusion-driven flow, as we will demonstrate in the following sections, the scaling relationship can differ. For instance, in some parameter limit, the self-similarity variable in the solution can be $y_1 t^{-1/4}$ for finite t. However, in this case, the derivatives of the averaged density still tend to be zero, and the higher-order derivatives become much smaller than the lower-order derivatives as $t \to \infty$.

The similar form of expansion (3.3) has found applications in various fields, including the modelling of chromatograph and reactors (Balakotaiah, Chang & Smith 1995), thin film fluid flows (Van Dyke 1987; Roberts 1996; Roberts & Li 2006) and shear dispersion of passive scalars (Gill 1967; Mercer & Roberts 1990; Young & Jones 1991; Ding & McLaughlin 2022*a*). A more rigorous foundation for this expansion can be established

through centre manifold theory (Carr 1979; Roberts 1988, 2014, 2015; Aulbach & Wanner 1996, 1999). For in-depth discussions on constructing centre manifolds, we refer interested readers to the cited literature, and we will not delve into the details here.

Another possible asymptotic expansion approach is a power series expansion involving a small parameter, denoted as ϵ, such as $c = \sum_{i=0}^{\infty} c_i \epsilon^i$. This approach is commonly used in multiscale analysis (Kondic 2003; Pavliotis & Stuart 2008; Wu & Chen 2014; Ding 2023). In this context, we highlight two advantages of the ansatz provided by (3.3) over the classical power series expansion for the specific problem addressed in this study.

First, in the classical ansatz, the coefficients remain independent of the small parameter ϵ. The quantity is expanded as a linear combination of ϵ powers. In contrast, in (3.3), the coefficients depend on small quantities, namely, the derivatives of the averaged scalar field. This nonlinear dependency enables us to achieve a more accurate approximation using fewer terms.

Second, when applying the standard multiscale analysis method to this problem, the results depend on the scaling relation between parameters. In the thin film limit, as we will discuss in § 5, the scalar field can be approximated as $c = c_0(y_1, t) + \epsilon c_2(y_1, y_3, t)$, where c_0 is the solution to a diffusion equation with a diffusivity of unity. In this scaling relation, the diffusion process is dominant, and the diffusion-driven flow does not have a first-order contribution. For cases where the diffusion-driven flow significantly enhances the dispersion of the stratified agent, an asymptotic analysis using a different scaling relation for physical parameters become necessary. In some cases, selecting the most appropriate characteristic parameter can be challenging. Additionally, since certain scales in the problem are time-dependent, the choice of scale may lead to time-dependent small parameters, which can complicate the development of a model that is uniformly valid across a wide range of parameter regimes.

In § 5, we will provide detailed explanations of the thin film approximation and discuss the differences between these two approaches.

3.2. *Leading-order term in asymptotic expansion*

The expansion (3.3) suggests that the deviation of the stratified scalar from its cross-sectional average is small. Consequently, this motivates us to examine the evolution equation for the cross-sectional averaged stratified scalar $\bar{c}$. Taking the cross-sectional average on both sides of the advection–diffusion equation (3.2) and utilizing the incompressibility condition and non-flux boundary condition yields

$$\partial_t \bar{c} + Pe \partial_{y_1} \overline{v_1 c} = \partial_{y_1}^2 \bar{c}. \tag{3.5}$$

Therefore, to obtain the leading-order approximation for the cross-sectional averaged stratified scalar, we need to compute $v_{1,0}$, $v_{1,1}$ and c_1 in the expansion (3.3).

There are some observations that can simplify the calculation of asymptotic expansion. Since the flow is induced via the density gradient, the fluid flow vanishes as $\partial_{y_1}\bar{c}$ vanishes. Therefore, $v_{1,0} = v_{3,0} = 0$. Substituting the expansion (3.3) into the continuity equation and noticing that $\partial_{y_1}(v_{1,1}\partial_{y_1}\bar{c}) = O(\partial_{y_1}^2 \bar{c})$, we obtain

$$\partial_{y_1} v_{1,0} + \partial_{y_3} v_{3,1} = 0. \tag{3.6}$$

Then to satisfy the no-slip boundary condition, $v_{3,1}$ must be zero.

Collecting the terms that are comparable to $\partial_{y_1}\bar{c}$ yields the following equation:

$$\left.\begin{array}{l} \dfrac{1}{Sc}\rho(\bar{c})\partial_t v_{1,1} = \partial_{y_3}^2 v_{1,1} - Re\,Ri\partial_c\rho(\bar{c})\left(c_1\sin\theta - \cos\theta\left(y_3 - \dfrac{1}{2}\right)\right), \\[2mm] \partial_t c_1 + Pe v_{1,1}\partial_{y_1}\bar{c} = \partial_{y_3}^2 c_1, \quad \partial_{y_3}c_1|_{y_3=0,1} = 0, \quad v_{1,1}|_{y_3=0,1} = 0. \end{array}\right\} \quad (3.7)$$

Previous studies (Kistovich & Chashechkin 1993; Ding & McLaughlin 2023) have uncovered fascinating dynamics in the time-dependent solution, particularly during short time scales when the initial velocity field is zero. However, these transient dynamics decay exponentially, and the solution converges to a steady-state either at the diffusion time scale or the viscosity time scale, depending on which of the two is larger. In many cases, the diffusion time scale significantly exceeds or is comparable to the viscosity time scale. For instance, in solute–liquid systems, the diffusivity of the solute molecule typically falls within the range of 10^{-5} cm^2 s^{-1}, while the kinematic viscosity of the liquid is around 10^{-2} cm^2 s^{-1}, resulting in a Schmidt number (Sc) of 10^3. In the case of temperature-stratified systems, the thermal diffusivity typically registers at approximately 10^{-3} cm^2 s^{-1}, with $Pr = 10$. In both cases, the diffusion time scale is much larger than the viscosity time scale. Therefore, given our specific interest in approximations at the diffusion time scale and to streamline our analysis without compromising accuracy, our primary focus will be on the steady-state solution of the aforementioned equation. By neglecting the time derivatives in (3.7), we arrive at the following non-homogeneous linear system for analysis:

$$\left.\begin{array}{l} 0 = \partial_{y_3}^2 v_{1,1} - Re\,Ri\partial_c\rho(\bar{c})(\sin\theta c_1 - \cos\theta(y_3 - \tfrac{1}{2})), \quad v_{1,1}|_{y_3=0,1} = 0, \\[2mm] Pe v_{1,1}\partial_{y_1}\bar{c} = \partial_{y_3}^2 c_1, \quad \partial_{y_3}c_1|_{y_3=0,1} = 0. \end{array}\right\} \quad (3.8)$$

Differencing the above equation twice with respect to y_3 yields

$$\left.\begin{array}{l} 0 = \partial_{y_3}^4 v_{1,1} - Re\,Ri\sin\theta\partial_c\rho\partial_{y_3}^2 c_1, \quad Pe\partial_{y_1}\bar{c}\partial_{y_3}^2 v_{1,1} = \partial_{y_3}^4 c_1, \\[2mm] \partial_{y_3}^3 v_{1,1}|_{y_3=0,1} = -Re\,Ri\partial_c\rho(\bar{c})\cos\theta. \end{array}\right\} \quad (3.9)$$

Then we can decouple the scalar field and velocity as

$$\left.\begin{array}{l} 0 = \partial_{y_3}^4 v_{1,1} - Re\,Pe\,Ri\sin\theta\partial_{y_1}\rho(\bar{c})v_{1,1}, \quad v_{1,1}|_{y_3=0,1} = 0, \\[2mm] \partial_{y_3}^3 v_{1,1}|_{y_3=0,1} = -Re\,Ri\partial_c\rho(\bar{c})\cos\theta, \\[2mm] \partial_{y_3}^4 c_1 = Re\,Pe\,Ri\partial_{y_1}\rho(\bar{c})(\sin\theta c_1 - \cos\theta(y_3 - \tfrac{1}{2})), \\[2mm] \partial_{y_3}c_1|_{y_3=0,1} = 0, \quad \partial_{y_2}^2 c_1|_{y_3=0,1} = 0, \end{array}\right\} \quad (3.10)$$

where we have used $\partial_{y_1}\rho(\bar{c}) = \partial_c\rho(\bar{c})\partial_{y_1}\bar{c}$ to simplify the equation. We can solve the equation and express $v_{1,1}, c_1$ in terms of $\partial_{y_1}\bar{c}$ as follows:

$$\left.\begin{array}{l} v_{1,1} = \dfrac{2\gamma\cot(\theta)}{Pe\partial_{y_1}\bar{c}}\dfrac{\sin(\gamma y_3)\sinh(\gamma(1-y_3)) - \sin(\gamma(1-y_3))\sinh(\gamma y_3)}{\sin(\gamma) + \sinh(\gamma)}, \\[4mm] c_1 = \cot\theta\left(y_3 - \dfrac{1}{2} - \dfrac{\cos(\gamma(1-y_3))\cosh(\gamma y_3) - \cos(\gamma y_3)\cosh(\gamma(1-y_3))}{\gamma(\sin(\gamma) + \sinh(\gamma))}\right), \end{array}\right\} \quad (3.11)$$

where $\gamma = (1/\sqrt{2})(-Re\,Pe\,Ri\sin\theta\partial_{y_1}\rho(\bar{c}))^{1/4}$. Recall our assumption of the stable density stratification, $\partial_{y_1}\rho(\bar{c}) \leq 0$, which implies that γ is a real non-negative number. In the case of linear density stratification, the equation above aligns with the steady solution previously presented in Phillips (1970) and Heitz et al. (2005).
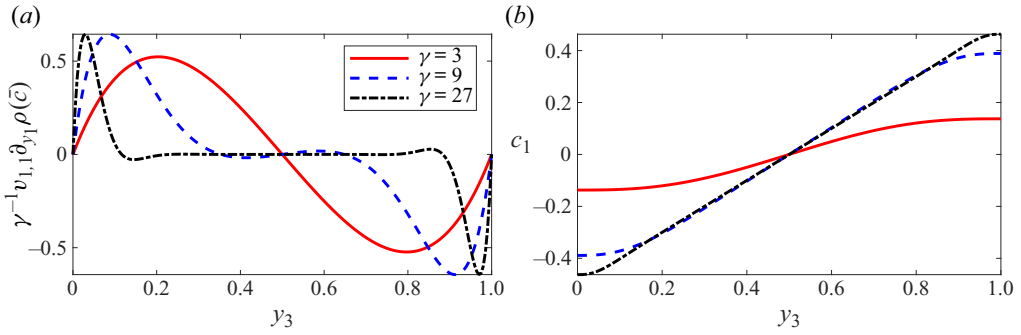
Figure 2. (a) Normalized leading-order approximation of the longitudinal velocity $v_{1,1}\partial_{y_1}\rho(\bar{c})/\gamma$ for various parameter γ. (b) Here c_1 for different γ.

As depicted in figure 2, both the normalized velocity $v_1\gamma^{-1} \approx v_{1,1}\partial_{y_1}\bar{c}\gamma^{-1}$ and c_1 are tightly confined within a narrow region near the boundary, especially when γ is large. The velocity is positive near $y_3 = 0$ indicating a upwelling flow near the upward facing boundary. Notably, the normalized velocity exhibits nearly uniform magnitude across different values of γ. Thus, γ^{-1} serves as an effective indicator of the boundary layer's thickness, and γ can be considered the characteristic velocity of the system. Moreover, the functions illustrated in figure 2 display an inherent odd symmetry about $y_3 = \frac{1}{2}$. This symmetry suggests that the leading-order approximations for both the velocity and density fields also possess odd symmetry with respect to $y_3 = \frac{1}{2}$. As a result, their cross-sectional averages inherently amount to zero.

As $\partial_{y_1}\bar{c} \to 0$, we have

$$v_{1,1} = -\frac{Re\,Ri y_3(y_3 - 1)(2y_3 - 1)\cos(\theta)\partial_c\rho}{12}$$
$$- \frac{Pe\,Re^2 Ri^2 y_3(2(y_3(2y_3 - 7) + 7)y_3^4 - 7y_3 + 3)\sin(2\theta)\partial_{y_1}\rho\partial_c\rho}{40\,320} + O((\partial_{y_1}\bar{c})^2),$$

(3.12)

and

$$c_1 = \frac{Pe\,Re\,Ri(1 - 2y_3^3(3y_3(2y_3 - 5) + 10))\cos(\theta)\partial_{y_1}\rho}{1440} + O((\partial_{y_1}\bar{c})^2).$$

(3.13)

Therefore $v_{1,1} \sim O(1)$, but $c_1 \sim O(\partial_{y_1}\bar{c})$. The leading-order approximation of the longitudinal velocity and the density field are given by $v_1 \sim v_{1,1}\partial_{y_1}\bar{c} = O(\partial_{y_1}\bar{c})$ and $c \sim c_1\partial_{y_1}\bar{c} = O((\partial_{y_1}\bar{c})^2)$, which confirms the ansatz of the asymptotic expansion (3.3).

Substituting the expansion of the velocity field and scalar field to (3.5) and noticing that $\bar{v}_{1,1} = 0$, the leading-order approximation reads

$$\partial_t\bar{c} + Pe\partial_{y_1}(\overline{v_{1,1}c_1}(\partial_{y_1}\bar{c})^2) = \partial_{y_1}^2\bar{c}.$$

(3.14)

Computing the average yields

$$\overline{v_{1,1}c_1} = \frac{-\cot^2(\theta)}{Pe\partial_{y_1}\bar{c}}\left(\frac{\sin(\gamma)\sinh(\gamma)}{(\sin(\gamma) + \sinh(\gamma))^2} + \frac{5(\cos(\gamma) - \cosh(\gamma))}{2\gamma(\sin(\gamma) + \sinh(\gamma))} + 1\right).$$

(3.15)

999 A12-10

The effective equation (3.14) for the averaged stratified scalar becomes

$$\left.\begin{aligned}
\partial_t \bar{c} &= \partial_{y_1}(\kappa_{eff} \partial_{y_1} \bar{c}), \\
\kappa_{eff} &= 1 + \cot^2(\theta)\left(\frac{\sin(\gamma)\sinh(\gamma)}{(\sin(\gamma)+\sinh(\gamma))^2} + \frac{5(\cos(\gamma)-\cosh(\gamma))}{2\gamma(\sin(\gamma)+\sinh(\gamma))} + 1\right).
\end{aligned}\right\} \tag{3.16}$$

This equation can be considered as an generalization of the diffusion equation with the constant diffusion coefficient replaced by a positive-definite function that depends on the derivative of the solution. This equation belongs to the family of equations that takes the form $\partial_t w = f(\partial_x w)\partial_x^2 w$, which occurs in the nonlinear theory of flows in porous media and also governs the motion of a nonlinear viscoplastic medium (see p. 342 in Polyanin & Zaitsev (2012)).

To complete the leading-order approximation for the whole system, we next consider the approximation for the transverse velocity and pressure. Once the leading-order approximation the longitudinal velocity is known, we can calculate the transverse velocity via the continuity equation. Substituting the expansion (3.3) into the continuity equation and collecting the terms that are comparable to $\partial_{y_1}^2 \bar{c}$ yields

$$\partial_{y_1}(v_{1,1}\partial_{y_1}\bar{c}) + \partial_{y_3}v_{3,2}\partial_{y_1}^2\bar{c} = 0. \tag{3.17}$$

Using no-slip boundary condition and the fact that $\bar{v}_{1,1} = 0$ yields the expression

$$\begin{aligned}
v_{3,2} &= -\frac{\displaystyle\int_0^{y_3} \partial_{y_1}(v_{1,1}\partial_{y_1}\bar{c})\,\mathrm{d}y_3}{\partial_{y_1}^2\bar{c}} \\
&= \frac{\cot(\theta)\gamma}{2Pe(\sin(\gamma)+\sinh(\gamma))^2\partial_{y_1}\rho}(\sin(\gamma(1-y))\sinh(\gamma y)(y\sin(\gamma) \\
&\quad + (y-1)\sinh(\gamma)) - \sin(\gamma y)\sinh(\gamma(1-y))((y-1)\sin(\gamma) + y\sinh(\gamma))).
\end{aligned} \tag{3.18}$$

In the limit $\partial_{y_1}\bar{c} \to 0$, we have

$$\begin{aligned}
v_{3,2} &= \frac{1}{24}Re\,Ri(y_3-1)^2 y_3^2 \cos(\theta) \\
&\quad + \frac{Pe\,Re^2 Ri^2 y_3^2(y_3-1)^2(3y_3^4 - 6y_3^3 - y_3^2 + 4y_3 + 9)\sin(2\theta)\partial_{y_1}\bar{\rho}}{120\,960} \\
&\quad + O((\partial_{y_1}\bar{c})^2). \tag{3.19}
\end{aligned}$$

Therefore, $v_3 \sim v_{3,2}\partial_{y_1}^2\bar{c} = O(\partial_{y_1}^2\bar{c})$, consistent with the assumption regarding the order of magnitude in the expansion given by (3.3).

The p_1 in the expansion of pressure provided in (3.3) satisfies

$$-\partial_{y_3}p_1 - Re\,Ri\cos\theta c_1\partial_c\rho(\bar{c}) = 0. \tag{3.20}$$

The solution is

$$\begin{aligned}
p_1 &= -\cot(\theta)\cos(\theta)RiRe\partial_c\rho\left(\frac{1}{12} + \frac{1}{2}(y-1)y\right. \\
&\quad \left. + \frac{\sin(\gamma - \gamma y)\cosh(\gamma y) - \cos(\gamma - \gamma y)\sinh(\gamma y) - \cos(\gamma y)\sinh(\gamma - \gamma y) + \sin(\gamma y)\cosh(\gamma - \gamma y)}{2\gamma^2(\sin(\gamma)+\sinh(\gamma))}\right).
\end{aligned} \tag{3.21}$$

In the limit $\partial_{y_1}\bar{c} \to 0$, we have

$$p_1 = \frac{\cos^2\theta\, Pe\, Re^2 Ri^2(28y_3^6 - 84y_3^5 + 70y_3^4 - 14y_3 + 3)\partial_{y_1}\rho\partial_c\rho}{20\,160} + O((\partial_{y_1}\bar{c})^2). \quad (3.22)$$

So far, we have derived the leading-order approximation for the entire system. The numerical simulations in the next section demonstrate that the leading-order approximation has decent accuracy in many scenarios. However, in cases of highly nonlinear scalar distribution, or where the density depends highly nonlinearly on the stratified scalar, higher-order terms are required to achieve desirable accuracy. Similar cases can be found in the previous literature. For example, Grayer *et al.* (2021) studied a stably stratified square cavity subjected to horizontal oscillations, which despite not being purely diffusion-driven, showed that approximations become less regular as viscosity decreases and how higher-order terms are needed.

3.3. *Numerical simulation*

In this subsection, we perform simulations of the full governing equation (2.6) to demonstrate both the accuracy and validity of our asymptotic approximation and the effective equation (3.16). The details of the numerical methods are documented in the Appendix. The computational domain is defined as $\{(y_1, y_3)|y_1 \in [-5, 5], y_3 \in [0, 1]\}$. The no-slip boundary condition is imposed for the velocity field, the no-flux boundary condition is imposed for the stratified scalar. The density and stratified scalar relation (2.9) is used for all test cases in this section.

In the first numerical simulation, the initial condition is

$$c_I = \frac{1}{2}\text{erfc}(y_1) - \frac{e^{-x^2}}{\sqrt{\pi}}\cos\theta\left(y_3 - \frac{1}{2}\right), \quad v_1 = v_3 = 0, \quad (3.23a,b)$$

and the dimensionless parameters are

$$Re = 1, \quad Ri\,Re = 12\,500, \quad Pe = 40, \quad Sc = 1, \quad \theta = \frac{\pi}{4}. \quad (3.24a\text{–}e)$$

The stratified scalar and velocity at $t = 0.04$ are depicted in figures 3(a i) and 3(b i), respectively. Since density gradient is large around $y_1 = 0$, the flow is also localized in that regime. Figures 3(a iii) and 3(b iii) display the density field and velocity field obtained by the simulation at $t = 2$. As time increases, the density field becomes smoother and a large fluid circulation is formed in this whole domain.

To proceed, we simulate the effective equation (3.16) with the same parameters (3.24a–e) for the comparison with the simulation of the governing equation (2.6). Figure 4(a) offers a comprehensive comparison. Here, we superimpose the solution of the effective equation with the cross-sectional averaged stratified scalar obtained through simulation of the complete governing equation (2.6) at the time instance $t = 2$. The remarkable alignment between these curves serves to underscore the accuracy of the effective equation as an adept approximation for the full system. Additionally, we include the solution corresponding to the pure diffusion equation (representing the case in the absence of fluid flow) within the same visual representation. Notably, the contrast between the pure diffusion solution and the effective equation's solution demonstrates a visible enhancement of fluid mixing through diffusion-driven flow.

Shifting our attention to figure 4(b), we delve into the temporal dynamics of the relative difference between the effective equation's solution and the full system's solution. At the
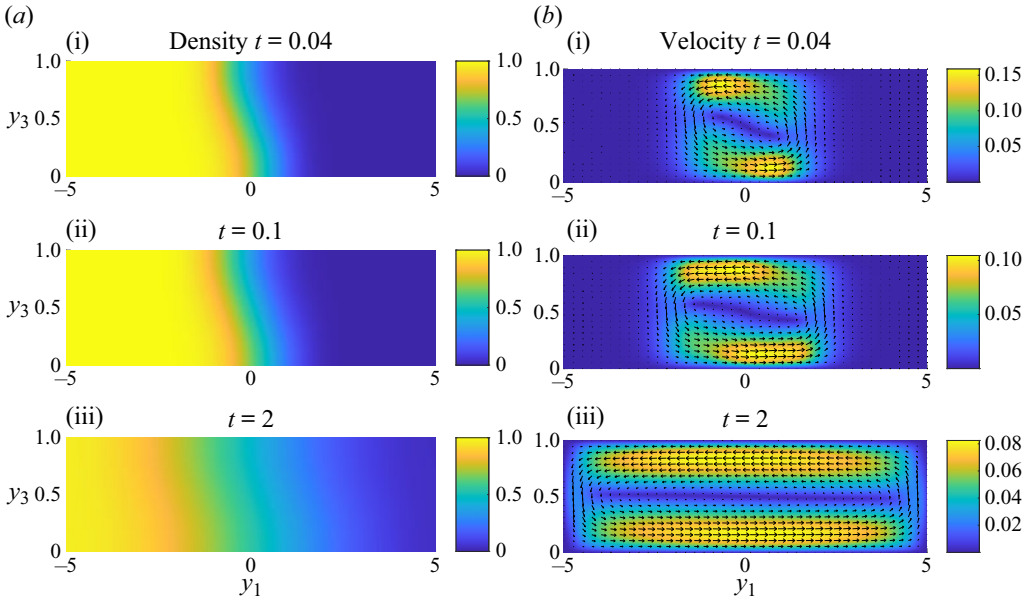
Figure 3. In (*a*), we display the density field at three time instances: $t = 0.04$ (i), $t = 0.1$ (ii) and $t = 2$ (iii). Panel (*b*) shows a pseudocolour plot illustrating the magnitude of the velocity field at the same time points. The initial condition and dimensionless parameter are provided in (3.23*a,b*) and (3.24*a–e*), respectively.
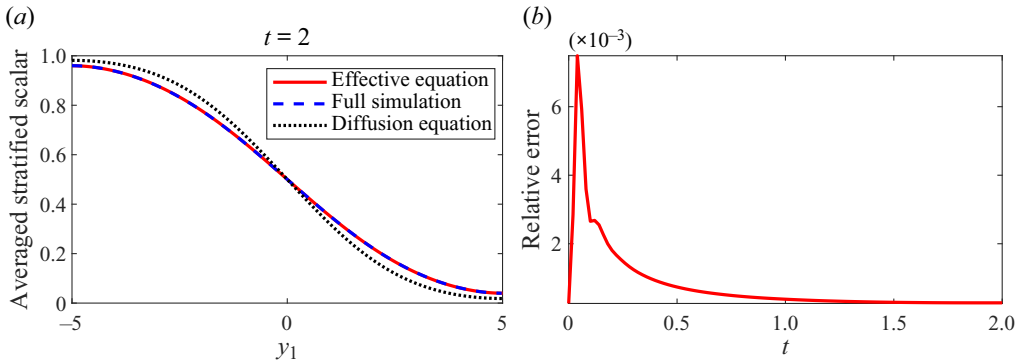

Figure 4. In (*a*), we present the solution of the effective equation (3.16) (represented by the red solid curve), the cross-sectional averaged stratified scalar derived from simulating the complete governing equation (illustrated by the blue dashed curve) and the solution to the diffusion equation (depicted by the black dotted curve) at the time instant $t = 2$ with parameters in (3.24*a–e*). In (*b*), we showcase the temporal evolution of the relative difference between the solution of the effective equation and the cross-sectional averaged stratified scalar obtained through the full simulation. This relative difference is defined as the maximum deviation between the functions across the domain divided by the maximum value of the averaged stratified scalar obtained from the full simulation.

inception ($t = 0$), this disparity is nil, attributed to identical initial conditions. During the initial stages, the relative difference magnifies as the system has yet to transition into the regime well-captured by the effective equation. Nevertheless, even during this phase, the maximum relative difference remains at approximately 0.0056. As the system approaches an asymptotic state, which occurs after the diffusion time scale ($t = 1$), the relative difference diminishes, stabilizing at around 0.001 until the simulation's culmination.
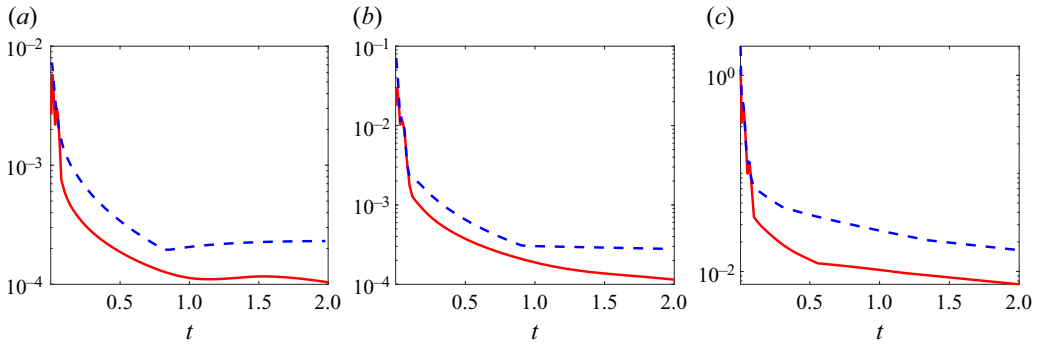
Figure 5. Comparison of the simulations with the initial condition in (3.23*a,b*), dimensionless parameter in (3.24*a–e*) and different $Sc = 1, 10, 100$: (*a*) difference in $\bar{c}$; (*b*) difference in scalar fields; (*c*) difference in velocity fields. The red curve depicts the relative difference between the solution for $Sc = 1$ and the solution for $Sc = 10$. The blue curve depicts the relative difference between the solution for $Sc = 1$ and the solution for $Sc = 100$.

It is worth noting that due to the assumption of the asymptotic analysis, the effective equation is valid for small density gradient $\partial_{y_1}\bar{c} \ll 1$. In this numerical test case, we have $\max_{y_1,t} \partial_{y_1}\bar{c} = 1/\sqrt{\pi} \approx 0.56419$, indicating that the parameter regime for the effective equation to reach a good approximation is larger than previously thought.

When deriving the effective equation in the previous section, we neglected the time derivative in (3.7). To verify the validity of this assumption, we conducted simulations with the same initial condition as in (3.23*a,b*) and parameters in (3.24*a–e*), but with different values of $Sc = 10, 100$. Figure 5 presents the relative differences in the scalar field, averaged scalar field, and velocity field between the solution for $Sc = 10, 100$ and the solution for $Sc = 1$. The relative differences for all three quantities are large at the early stage but quickly decreases as time increases. At the diffusion time scale, the relative difference in scalar field is around 10^{-4} and the relative difference in velocity field is around 10^{-2}, which approach the maximum accuracy achievable with the numerical scheme and resolution used in the simulation. This observation suggest that the value of Sc does not have a significant impact on the scalar field and velocity field at the diffusion time scale, justifying the neglect of the time derivative in (3.7) for $Sc \geq 1$.

To demonstrate the validity of the effective equation across a wide range of parameters, we conducted a simulation with the same initial condition (3.23*a,b*) and a different set of non-dimensional parameters,

$$Re = 0.1, \quad Ri\,Re = 100\,000, \quad Pe = 100, \quad Sc = 1, \quad \theta = \frac{\pi}{4}. \qquad (3.25a\text{–}e)$$

The velocity field results are presented in figure 6(*a*) and figure 6(*b* i). Comparing figure 3 with figure 6, we make three observations: first, as Ri increases, the velocity field exhibits more intricate structures during the initial stages. A distinctive 'S' shape curve forms in the pseudocolour plot of the velocity field around $t = 0.08$ and persists in subsequent time instants. Second, the flow is more confined near the boundary, which is consistent with the observation we made from figure 2. Third, at $t = 1$, figure 3(*b*) illustrates that the velocity field is antisymmetric with respect to $y_3 = \frac{1}{2}$. However, in figure 6(*b*), at $t = 1$, the velocity field is not antisymmetric with respect to $y_3 = \frac{1}{2}$ near the two ends of the domain $y_1 = \pm 5$.
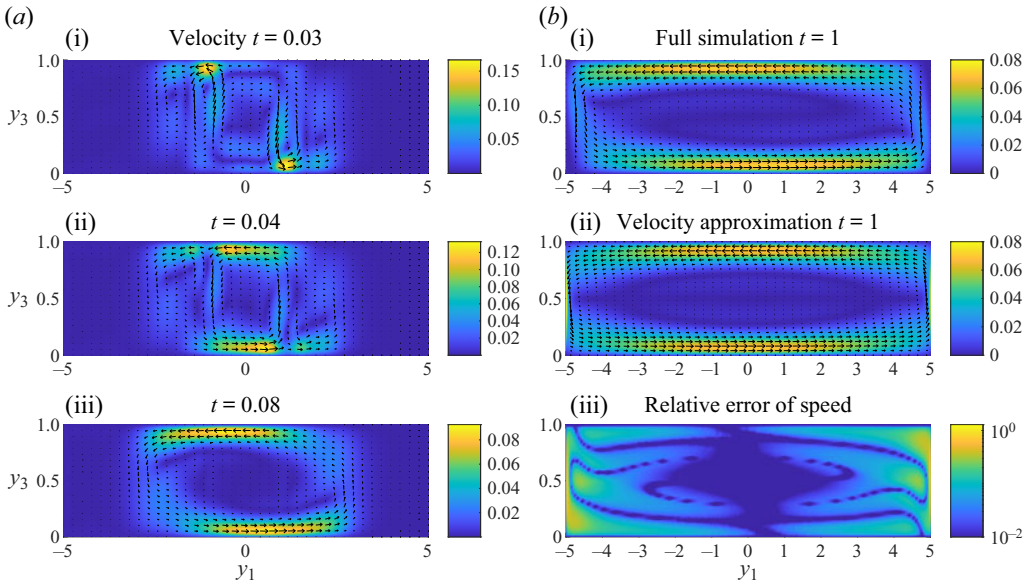
999 A12-14

Figure 6. In (*a*), a pseudocolour plot illustrates the magnitude of the velocity field with parameters in (3.25*a–e*) at three time instances: $t = 0.03$ (i), $t = 0.04$ (ii) and $t = 0.08$ (iii). In (*b*), the subpanel (i) displays the velocity field at $t = 1$; (ii) showcases the velocity field approximation at $t = 1$, calculated using (3.11) and (3.19); (iii) depicts the relative approximation error of the speed.

Figure 6(*b* ii,iii) depict the approximation of the velocity field and the corresponding relative error at $t = 1$. While the error remains relatively small within the interior of the domain, it increases notably near the corners and becomes significantly large in the narrow regions adjacent to the left- and right-hand boundaries, with the layer thickness approximately 0.05. This discrepancy stems from two main reasons. First, the leading-order approximation of velocity exhibits antisymmetry across the entire domain, whereas the actual velocity field does not possess this property. Second, the asymptotic approximation outlined in the previous section holds true for an infinite domain. However, in a confined domain, the no-slip boundary condition for the velocity field at the end of the domain ($y_3 = \pm 5$) is required but was not enforced during the derivation of the asymptotic approximation. While the no-flux boundary condition for the stratified scalar ensures a longitudinal velocity component of zero, the transverse velocity could deviate from zero where it should be, resulting in a significant error near the boundary. Achieving a more uniform approximation over the domain necessitates incorporating boundary layer corrections near the boundary into the velocity approximation.

One might assume that the substantial error in velocity approximation near the left- and right-hand ends of the domain could significantly compromise the accuracy of other approximations. However, as depicted in figure 7(*a*), the solution of the effective equation perfectly overlaps with the averaged scalar field obtained from the full simulation. This alignment is further confirmed in figure 7(*b*), illustrating the temporal dynamics of the relative difference, which remains small throughout the entire time interval. We believe this is due to two possible reasons: first, the error in the velocity field approximation is localized near the ends of the domain. Since the domain is long and narrow, the boundary layer constitutes a relatively small portion of the overall domain, consequently having a limited impact on the entire dynamic process. For a domain with comparable length scales
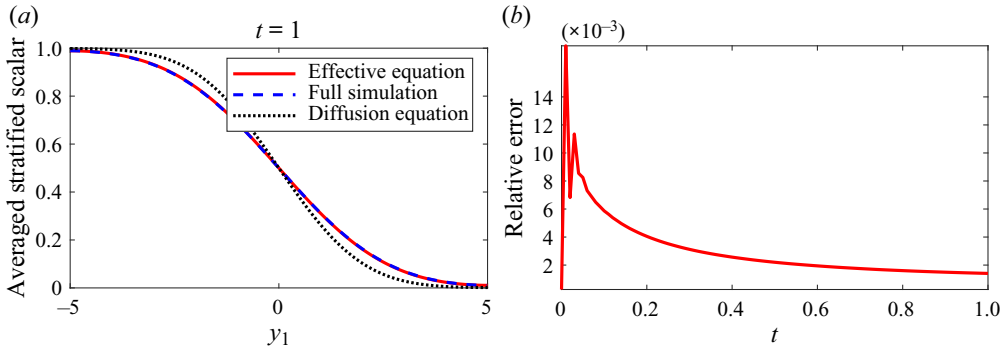
999 A12-15

Figure 7. In (*a*), we present the solution of the effective equation (3.16) (represented by the red solid curve) with parameters in (3.25*a–e*), the cross-sectional averaged stratified scalar derived from simulating the complete governing equation (illustrated by the blue dashed curve) and the solution to the diffusion equation (depicted by the black dotted curve) at the time instant $t = 1$. Panel (*b*) showcases the temporal evolution of the relative difference between the solution of the effective equation and the cross-sectional averaged stratified scalar obtained through the full simulation.

in both directions, the error in the velocity field approximation may lead to a substantial error in the scalar field approximation. Second, only the longitudinal component of the velocity contributes to the scalar transport in the leading-order approximation. Therefore, the error in the transverse component of velocity does not undermine the accuracy of the effective equation.

Last, we consider a staircase-like profile as the initial condition, a feature commonly encountered in certain oceanographic scenarios

$$
\left.
\begin{aligned}
c_I &= f(y_1) + \partial_{y_1} f(y_1) \cos\theta \left(y_3 - \frac{1}{2} \right), \quad f(y_1) = \frac{\mathrm{erfc}(y_1 + \frac{5}{2}) + \mathrm{erfc}(y_1 - \frac{5}{2})}{4}, \\
v_1 &= v_3 = 0.
\end{aligned}
\right\}
$$
(3.26)

The non-dimensional parameters are provided in (2.8*a–d*), and $\theta = \pi/4$.

The velocity field results are depicted in figure 8. At the early phase ($t = 0.01$), multiple convection cells emerge. The adjacent cells have differing orientations. These cells swiftly amalgamate into two larger convection cells with the same anticlockwise orientation, located where the initial profile exhibits significant gradients. As the density distribution becomes smoother, around $t = 0.2$, the merging of the two convection cells initiates. By $t = 1$, only a single convection cell remains. The velocity distribution closely resembles that of simulations with differing initial conditions. Figure 8(*b* iii) illustrates the disparity between the solutions of the effective equation and the cross-sectional averaged stratified scalar obtained through the full simulation. The small relative difference again demonstrates the validity of the effective equation.

4. Analysis of the effective equation

After confirming the accuracy of the effective equation (3.16) for the stratified scalar through numerical simulations, this section delves deeper into its properties.
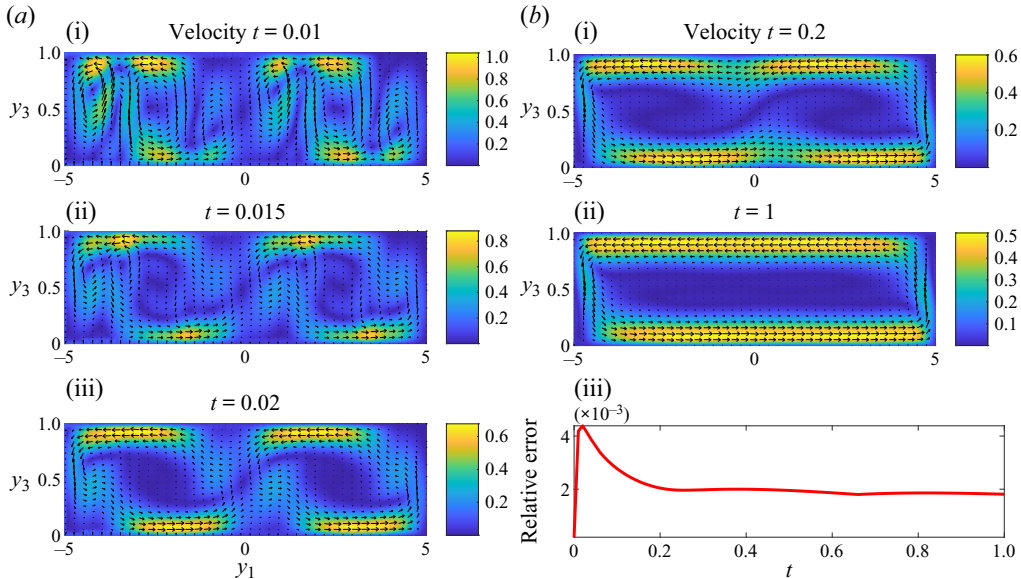
Figure 8. A pseudocolour plot illustrates the magnitude of the velocity field with the initial condition (3.26) and parameters in (2.8*a*–*d*) at different time instances. Subpanel (*b* iii) showcases the temporal evolution of the relative difference between the solution of the effective equation and the cross-sectional averaged stratified scalar obtained through the full simulation.

The behaviour of (3.16) is primarily governed by κ_{eff}. Its asymptotic expansions for small and large values of γ are provided as follows:

$$\left.\begin{array}{l} \kappa_{eff} = 1 + \cot^2(\theta)\left(\left(1 - \dfrac{5}{2\gamma}\right) + \dfrac{(2\gamma + 5)\sin(\gamma) + 5\cos(\gamma)}{\gamma\,\mathrm{e}^\gamma} + O(\mathrm{e}^{-2\gamma})\right), \quad \gamma \to \infty, \\[4mm] \kappa_{eff} = 1 + \cot^2(\theta)\left(\dfrac{\gamma^8}{22680} - \dfrac{2879\gamma^{12}}{4086482400} + O(\gamma^{16})\right), \quad \gamma \to 0. \end{array}\right\} \tag{4.1}$$

Figure 9 shows the graph of $(\kappa_{eff} - 1)/\cot^2(\theta)$ and its approximations as a function of γ. By examining both the graph and the asymptotic approximations, we can conclude that for $\gamma \geq 0$:

$$1 \leq \kappa_{eff}(\gamma) < 1 + \cot^2(\theta). \tag{4.2}$$

For large values of γ, (3.16) becomes a diffusion equation with an enhanced diffusion coefficient:

$$\partial_t \bar{c} = (1 + \cot^2\theta)\partial_{y_1}^2 \bar{c}. \tag{4.3}$$

This resembles the scenario of a passive scalar governed by an advection–diffusion equation with a prescribed velocity field. In the context of the channel domain and at diffusion time scales, the advection–diffusion equation can be effectively simplified to a diffusion equation with an enhanced effective diffusion coefficient (see Chatwin (1970), Smith (1982), Young & Jones (1991), Ding *et al.* (2021) and Ding & McLaughlin (2022*b*) for related work).

However, it is important to note that γ is not a constant – it depends on the density gradient. Therefore, the diffusion equation (4.3) cannot provide a uniform approximation
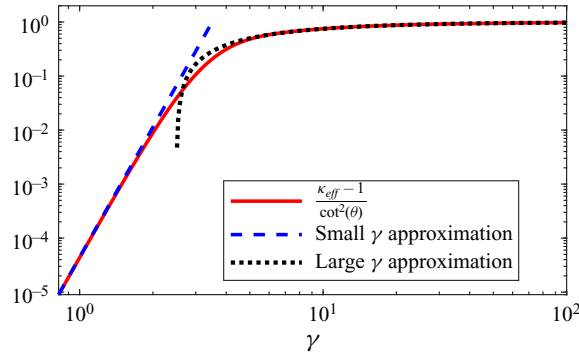
Figure 9. The red solid curve represents $(\kappa_{eff} - 1)/\cot^2(\theta)$ as a function of the non-dimensional parameter $\gamma = (1/\sqrt{2})(-Re\,Pe\,Ri\sin\theta\,\partial_{y_1}\bar{\rho})^{1/4}$. For small values of γ, the corresponding approximation is $\gamma^8/22\,680$, which is depicted by the blue dashed curve. Conversely, for large values of γ, the corresponding approximation is $1 - 5/2\gamma$, illustrated by the black dotted curve.
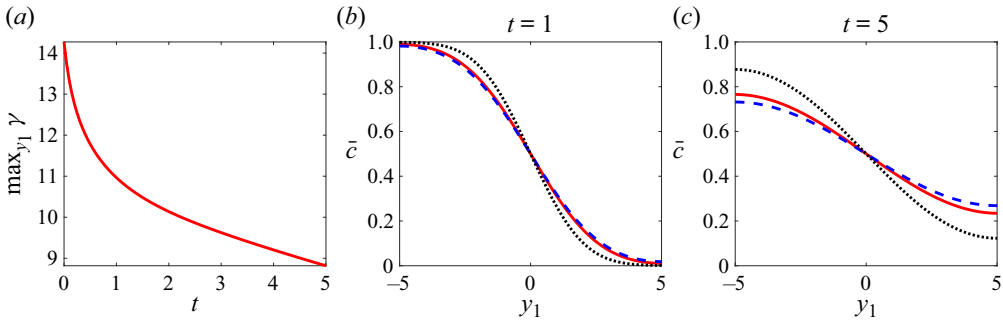

Figure 10. Panel (*a*) shows $\max_{y_1}\gamma$ as a function of time in the simulation with the parameters provided in (3.25*a–e*). Panel (*b*) presents the solution of the effective equation (3.16) (represented by the red solid curve), the solution of diffusion equation with diffusivity $1 + \cot^2(\theta)$ (illustrated by the blue dashed curve) and the solution to the diffusion equation with diffusivity 1 (depicted by the black dotted curve) at the time instant $t = 1$. Panel (*c*) shows the corresponding curves at the time instant $t = 5$.

of the effective equation for all time instances. As time progresses, the stratified scalar becomes more homogeneous across the domain. As the density gradient decreases, γ decreases, and the approximation given by (4.3) becomes less accurate.

To illustrate this, we conducted simulations with the parameters provided in (3.25*a–e*) as an example. Figure 10(*a*) shows the maximum value of γ across the domain as a function of time. As we expect, it is a decreasing function. Figure 10(*b*) demonstrates that the solution to the diffusion equation (4.3) reasonably approximates the solution to the effective equation (3.16) initially. However, as time progresses and the density gradient decreases, $\max_{y_1}\gamma$ also decreases. At $t = 5$, the difference between the solution of (4.3) and that of (3.16) becomes more pronounced. This example also demonstrates that a single diffusion equation is not enough to accurately describes the dynamics of the averaged stratified scalar at all different time scale.

Equation (4.3) suggests that as the inclination angle approaches zero, the dispersion rate may increase, possibly reaching infinity. It is crucial to emphasize that this conclusion holds true only when other parameters are kept constant. It is worth noting that as the inclination angle decreases, maintaining the same value of γ necessitates keeping the same

999 A12-18

density variation in the y_1 direction, which in turn requires a larger density variation in the x_3 direction. Achieving such a condition in practical applications can pose significant challenges.

Next, we consider the case with small γ. In this limit, the effective equation for the stratified scalar (3.16) reduces to

$$\partial_t \bar{c} = \partial_{y_1} \left(\left(1 + \left(\frac{Ri \, Pe \, Re \cos(\theta)}{72\sqrt{70}} \partial_{y_1} \rho(\bar{c}) \right)^2 \right) \partial_{y_1} \bar{c} \right). \tag{4.4}$$

The closed form expression of the solution of this equation is not available. However, we can obtain the solution in some limits for unbounded domain. When the nonlinear term is much larger than the diffusion term, namely, $(Ri \, Pe \, Re \cos(\theta)/72\sqrt{70})\partial_{y_1}\rho(\bar{c}) \gg 1$, and $\partial_c \rho$ is a constant, (4.4) can be approximated by

$$\partial_t \bar{c} = \partial_{y_1}(\alpha^2 (\partial_{y_1}\bar{c})^3), \quad \alpha = \frac{Ri \, Pe \, Re \cos(\theta)\partial_c \rho}{72\sqrt{70}}. \tag{4.5}$$

We can look for the self-similarity solution, $c(y_1, t) = f(\xi)$, where $\xi = t y_1^{-1/4}$. Equation (4.5) becomes

$$f'(\xi)(12\alpha^2 f'(\xi)f''(\xi) + \xi) = 0. \tag{4.6}$$

The solution is

$$f(\xi) = \begin{cases} C_2 + \pi C_1 \alpha \sqrt{3} & \xi \geq 2\alpha\sqrt{6C_1}, \\ C_2 - \dfrac{\dfrac{1}{2}\xi\sqrt{24\alpha^2 c_1 - \xi^2} + 12\alpha^2 c_1 \tan^{-1}\left(\dfrac{\xi}{\sqrt{24\alpha^2 c_1 - \xi^2}}\right)}{2\sqrt{3}\sqrt{\alpha}} & -2\alpha\sqrt{6C_1} \leq \xi \leq 2\alpha\sqrt{6C_1}, \\ C_2 - \pi c_1 \alpha \sqrt{3} & \xi \leq -2\alpha\sqrt{6C_1}, \end{cases} \tag{4.7}$$

where C_1, C_2 are the constants that can be defined by the boundary condition at infinity. For the case $\bar{c}(\infty) = 0$ and $\bar{c}(-\infty) = 1$, we have $C_1 = 1/2\sqrt{3}\pi\alpha$, $C_2 = \frac{1}{2}$. Notice that the similarity variable for the pure diffusion equation is $\xi = y_1/\sqrt{t}$. Therefore, $t \to \infty$, the neglected diffusion term in the above calculation becomes dominant eventually.

Last, we can represent γ in terms of the physical parameters as follows: $\gamma = (1/\sqrt{2})((gH^3\rho_0/\kappa\mu)\sin\theta\partial_{y_1}\rho(\bar{c}))^{1/4}$. Therefore, smaller diffusivity, lower viscosity, greater gravitational constant, larger gap thickness and higher density result in a larger value of γ. We can calculate γ using the practical parameters provided in (2.8a–d). If we set $\theta = \pi/4$ and estimate the density gradient as $\partial_{y_1}\rho(\bar{c}) = \sin\theta\partial_{x_3}\rho(\bar{c})$, we obtain $\gamma \approx 8.94506$ and $\kappa_{eff}(\gamma) \approx 1.720605$. With the same parameters and a smaller inclination angle $\theta = \pi/10$, we have $\gamma \approx 5.91333$ and a larger effective diffusivity $\kappa_{eff}(\gamma) \approx 6.46129$. In these cases, we cannot employ the approximate equations (4.3) and (4.4). Instead, we must use the complete effective equation (3.16) to solve for the stratified scalar.

4.1. *Long time behaviour of the solution*

As demonstrated in our previous examples, diffusion-driven flow enhances the mixing of a stratified scalar at some time scales. One might expect the difference between the density
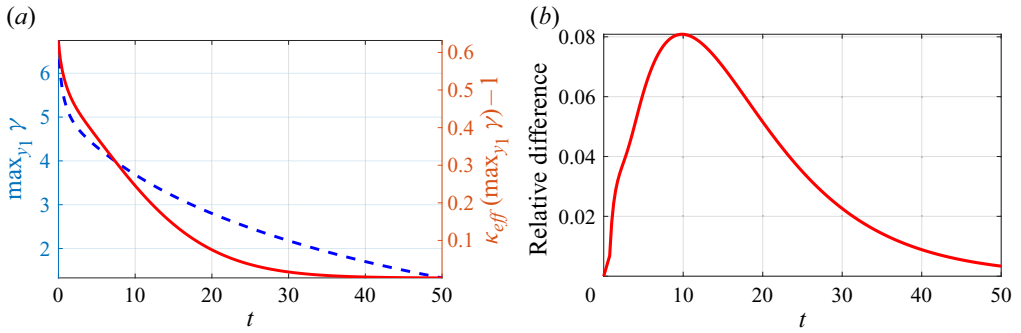
Figure 11. (*a*) The blue dashed curve represents $\max_{y_1} \gamma$ and is associated with the left-hand y axis. The red solid curve represents $\kappa_{eff}(\max_{y_1} \gamma) - 1$ and is associated with the right-hand y axis. (*b*) The relative difference between the density profile with and without the fluid as a function of time. The parameters used in the simulation are provided in (3.24*a*–*e*).

profile with and without the fluid to increase as time progresses or at least persist at long times. However, intriguingly, this difference actually vanishes over extended periods.

To understand this, it is essential to recall an interesting observation that emerges when considering different solutions to the same diffusion equation. Under some conditions, these solutions converge to a self-similarity solution asymptotically at long times, as discussed in Newman (1984). To illustrate this point, consider two solutions: $f_1 = \frac{1}{2}\mathrm{erfc}(x/2\sqrt{t})$ and $f_2 = \frac{1}{2}\mathrm{erfc}(x/2\sqrt{\sigma^2 + t})$, both satisfying the diffusion equation $\partial_t f = \partial_x^2 f$. Although they begin with different initial conditions, the relative difference between them diminishes as $t \to \infty$:

$$\frac{f_1 - f_2}{f_1} = \frac{\sigma^2 x t^{-3/2}}{2\sqrt{\pi}} + O(t^{-2}). \tag{4.8}$$

The time scale for this convergence depends on the difference in the initial conditions and can be multiple times the diffusion time scale.

This observation implies that even if diffusion-driven flow initially amplifies the dispersion of the stratified agent, when the density gradient is sufficiently weak, the governing equation for the stratified scalar approximates a diffusion equation with a diffusivity of unity. While some disparity remains between the solution of the effective equation and the solution of the pure diffusion equation, this difference diminishes over longer time scales.

To confirm this conclusion, we solve the effective equation (3.16) with parameters provided in (3.24*a*–*e*). In figure 11(*a*), we plot $\max_{y_1} \gamma$ and $\kappa_{eff}(\max_{y_1} \gamma) - 1$ as functions of time, providing an estimation of the enhancement of dispersion induced by diffusion-driven flow. We observe that the enhanced diffusivity decreases below 0.1 after $t > 20$, which implies the effective equation is close to the pure diffusion equation after that time. In figure 11(*b*), we display the relative difference between the density profiles with and without flow. This difference initially increases, reaching its maximum around $t = 10$, but subsequently decreases to 0.003 at $t = 50$.

This result demonstrates that in a confined domain with no-flux boundary condition, the density profile in a system with the diffusion driven flow asymptotically converges to the one without the flow at extremely large time scale.

999 A12-20

5. Comparison with the thin film approximation

As previously mentioned, we can employ the classical asymptotic expansion to analyse the governing equation (2.6). In this section, we will utilize the thin film approximation and subsequently compare the results with those obtained previously.

In the thin film approximation, we select distinct length scales in different directions for the purpose of non-dimensionalization:

$$
\left.
\begin{aligned}
& Ly_1' = y_1, \quad Hy_3' = y_3, \quad V_i v_i' = v_i, \quad \frac{\rho_0 LvU}{H^2} p' = p, \quad \frac{L^2}{\kappa} t' = t, \quad \rho_0 \rho' = \rho, \\
& c_0 c' = c, \quad \epsilon = \frac{V_3}{V_1} = \frac{H}{L} \ll 1, \quad Re = \frac{V_1 H}{v}, \quad Pe = \frac{V_1 H}{\kappa}, \quad Sc = \frac{\mu}{\rho_0 \kappa}, \quad Ri = \frac{Hg}{V_1^2}.
\end{aligned}
\right\}
\tag{5.1}
$$

The non-dimensionalized governing equation becomes

$$
\left.
\begin{aligned}
& \rho'\left(\frac{\epsilon^2}{Sc}\partial_{t'} v_1' + \epsilon Re(v_1' \partial_{y_1'} v_1' + v_3' \partial_{y_3'} v_1')\right) = (\epsilon^2 \partial_{y_1'}^2 v_1' + \partial_{y_3'}^2 v_1') - \partial_{y_1'} p' - Re\,Ri\rho' \sin\theta, \\
& \rho'\left(\frac{\epsilon^3}{Sc}\partial_{t'} v_3' + \epsilon^2 Re(v_1' \partial_{y_1'} v_3' + v_3' \partial_{y_3'} v_3')\right) = (\epsilon^3 \partial_{y_1'}^2 v_3' + \epsilon \partial_{y_3'}^2 v_3') - \frac{1}{\epsilon}\partial_{y_3'} p' - Re\,Ri\rho' \cos\theta, \\
& \epsilon^2 \partial_{t'} c' + \epsilon Pe v_1' \partial_{y_1'} c' + \epsilon Pe v_3' \partial_{y_3'} c' = \epsilon^2 \partial_{y_1'}^2 c' + \partial_{y_3'}^2 c', \\
& \partial_{y_1'} v_1' + \partial_{y_3'} v_3' = 0.
\end{aligned}
\right\}
\tag{5.2}
$$

Dropping primes and rearranging the equation results in

$$
\left.
\begin{aligned}
& \rho\left(\frac{\epsilon^2}{Sc}\partial_t v_1 + \epsilon Re(v_1 \partial_{y_1} v_1 + v_3 \partial_{y_3} v_1)\right) = (\epsilon^2 \partial_{y_1}^2 v_1 + \partial_{y_3}^2 v_1) - \partial_{y_1} p - Re\,Ri\rho \sin\theta, \\
& \rho\left(\frac{\epsilon^4}{Sc}\partial_t v_3 + \epsilon^3 Re(v_1 \partial_{y_1} v_3 + v_3 \partial_{y_3} v_3)\right) = \epsilon^2(\epsilon^2 \partial_{y_1}^2 v_3 + \partial_{y_3}^2 v_3) - \partial_{y_3} p - \epsilon Re\,Ri\rho \cos\theta, \\
& \epsilon^2 \partial_t c + \epsilon Pe(v_1 \partial_{y_1} c + v_3 \partial_{y_3} c) = \epsilon^2 \partial_{y_1}^2 c + \partial_{y_3}^2 c, \\
& \partial_{y_1} v_1 + \partial_{y_3} v_3 = 0.
\end{aligned}
\right\}
\tag{5.3}
$$

We consider the formal power series expansions for the velocity, stratified scalar and pressure:

$$
v_i = \sum_{k=0}^{\infty} v_{i,k} \epsilon^k, \quad c = \sum_{k=0}^{\infty} c_k \epsilon^k, \quad p = \sum_{k=0}^{\infty} p_k \epsilon^k, \quad \rho(c) = \sum_{k=0}^{\infty} \rho_k \epsilon^k.
\tag{5.4a–d}
$$

We have $v_{i,k}|_{y \in \partial\Omega} = 0$ from the no-slip boundary condition of the velocity field, and $\partial_n c_k|_{y \in \partial\Omega} = 0$ from the no-flux boundary condition of the stratified scalar. The coefficient in the expansion of ρ can be calculated from c_k and the Taylor expansion of $\rho(c)$.

Substituting the expansion into the governing equation and collecting $O(1)$ terms yield the following equation:

$$
0 = \partial_{y_3}^2 v_{1,0} - \partial_{y_1} p_0 - Re\,Ri\rho_0 \sin\theta, \quad 0 = \partial_{y_3} p_0, \quad 0 = \partial_{y_3}^2 c_0, \quad \partial_{y_1} v_{1,0} + \partial_{y_3} v_{3,0} = 0.
\tag{5.5}
$$

There are two possible group of solutions,

$$
v_{1,0} = v_{3,0} = 0, \quad p_0 = Re\,Ri\sin\theta \int_0^{y_1} \rho_0 \, dy_1,
\tag{5.6a,b}
$$

999 A12-21

and

$$v_{1,0} = Cy_3(y_3 - 1), \quad v_{3,0} = 0, \quad p_0 = -2Cy_1 + Re\,Ri\sin\theta \int_0^{y_1} \rho_0 \, dy_1, \quad (5.7a\text{–}c)$$

where C is a constant number and c_0, ρ_0 are independent of y_3. The second solution describes a flow generated by a constant pressure gradient, which does not represent the correct physical problem. Therefore, we regard the first solution as the correct leading-order approximation.

Collecting the terms that is comparable to $O(\epsilon)$ yields the following equation:

$$\left.\begin{array}{c} Re\rho_0(v_{1,0}\partial_{y_1}v_{1,0} + v_{3,0}\partial_{y_3}v_{1,0}) = \partial_{y_3}^2 v_{1,1} - \partial_{y_1}p_1 - Re\,Ri\rho_1\sin\theta, \\ 0 = -\partial_{y_3}p_1 - Re\,Ri\rho_0\cos\theta, \quad Pe(v_{1,0}\partial_{y_1}c_0 + v_{3,0}\partial_{y_3}c_0) = \partial_{y_3}^2 c_1, \\ \partial_{y_1}v_{1,1} + \partial_{y_3}v_{3,1} = 0. \end{array}\right\} \quad (5.8)$$

Using the conclusions (5.6a,b) reduces the above equation to

$$\left.\begin{array}{c} 0 = \partial_{y_3}^2 v_{1,1} - \partial_{y_1}p_1 - Re\,Ri\rho_1\sin\theta, \quad 0 = -\partial_{y_3}p_1 - Re\,Ri\rho_0\cos\theta, \\ 0 = \partial_{y_3}^2 c_1, \quad \partial_{y_1}v_{1,1} + \partial_{y_3}v_{3,1} = 0. \end{array}\right\} \quad (5.9)$$

Similar to the equation for $O(1)$ terms, the solution is not unique. To eliminate the solution representing the pressure driven flow, we impose the condition $\bar{p}_1 = 0$. From the second equation, we have

$$p_1 = -(y_3 - \tfrac{1}{2})Re\,Ri\rho_0\cos\theta. \quad (5.10)$$

Since c_1 is independent of y_3, it follows that $\rho_1 = c_1\partial_c\rho(c_0)$ is also independent of y_3. Averaging the first equation yields $\bar{v}_{1,1} = 0$. Differentiating the first equation in (5.9) with respect to y_3 twice give us

$$0 = \partial_{y_3}^4 v_{1,1}, \quad v_{1,1}|_{y=0,1} = 0, \quad \partial_{y_3}^3 v_{1,1}|_{y=0,1} = -Re\,Ri\cos\theta\partial_{y_1}\rho_0. \quad (5.11a\text{–}c)$$

The solution is

$$v_{1,1} = -Re\,Ri\cos\theta\partial_{y_1}\rho_0\frac{y_3(y_3 - 1)(2y_3 - 1)}{12}, \quad (5.12)$$

which is consistent with the first term in (3.12). It is important to note that the definition of $v_{1,1}$ in (3.12) differs from the one presented here. To make a comparison, $v_{1,1}$ in (3.12) need to be multiplied with $\partial_{y_1}\bar{c}$.

From the third equation in (5.9), we conclude that c_1 is independent of y_3. Moreover, after substituting the expression of $v_{1,1}$ back to the first equation in (5.9), we obtain $\rho_1 = 0$. The continuity equation gives us the expression of $v_{3,1}$, as follows:

$$v_{3,1} = -\int_0^{y_3} \partial_{y_1}v_{1,1} \, dy_3 = Re\,Ri\cos\theta\partial_{y_1}^2\rho_0\frac{y_3^2(y_3 - 1)^2}{24}, \quad (5.13)$$

which is consistent with the first term in (3.19).

999 A12-22

Collecting the terms that are comparable to $O(\epsilon^2)$ yields the following equation:

$$
\left.
\begin{aligned}
\frac{\rho_0}{Sc}\partial_t v_{1,0} + Re\rho_0(v_{1,0}\partial_{y_1}v_{1,1} + v_{1,1}\partial_{y_1}v_{1,0} + v_{3,0}\partial_{y_3}v_{1,1} + v_{3,1}\partial_{y_3}v_{1,0}) \\
+ Re\rho_1(v_{1,0}\partial_{y_1}v_{1,0} + v_{3,0}\partial_{y_3}v_{1,0}) = (\partial_{y_1}^2 v_{1,0} + \partial_{y_3}^2 v_{1,2}) - \partial_{y_1}p_2 - Re\,Ri\rho_2\sin\theta, \\
0 = \partial_{y_3}^2 v_{3,0} - \partial_{y_3}p_2 - Re\,Ri\rho_1\cos\theta, \\
\partial_t c_0 + Pe(v_{1,0}\partial_{y_1}c_1 + v_{1,1}\partial_{y_1}c_0 + v_{3,0}\partial_{y_3}c_1 + v_{3,1}\partial_{y_3}c_0) = \partial_{y_1}^2 c_0 + \partial_{y_3}^2 c_2, \\
\partial_{y_1}v_{1,2} + \partial_{y_3}v_{3,2} = 0.
\end{aligned}
\right\}
$$

$$(5.14)$$

Using the current conclusions for $O(\epsilon)$ terms, the above equation reduces to

$$
\left.
\begin{aligned}
0 = \partial_{y_3}^2 v_{1,2} - \partial_{y_1}p_2 - Re\,Ri\rho_2\sin\theta, \quad 0 = -\partial_{y_3}p_2 - Re\,Ri\rho_1\cos\theta, \\
\partial_t c_0 + Pe v_{1,1}\partial_{y_1}c_0 = \partial_{y_1}^2 c_0 + \partial_{y_3}^2 c_2.
\end{aligned}
\right\}
$$

$$(5.15)$$

Notice that $\int_0^1 v_{1,1}\,\mathrm{d}y_3 = 0$ and c_0 is independent of y_3. Integrating on both sides of the last equation in (5.15) with respect to y_3 and using the no-flux boundary conditions yields the evolution equation for c_0: $\partial_t c_0 = \partial_{y_1}^2 c_0$.

Now the last equation in (5.15) becomes $Pe v_{1,1}\partial_{y_1}c_0 = \partial_{y_3}^2 c_2$ and implies

$$
c_2 = \frac{Pe\,Re\,Ri(1 - 2y_3^3(10 + 3y_3(2y_3 - 5)))\cos(\theta)\partial_{y_1}c_0\partial_{y_1}\rho_0}{1440},
$$

$$(5.16)$$

which is consistent with the second term in (3.13). It is important to note that the definition of c_1 in § 3 differs from the one presented here.

The stratified scalar approximation is expressed as $c = c_0 + \epsilon^2 c_2 + O(\epsilon^3)$, which serves as the solution to a pure diffusion equation augmented by a higher-order correction term. The fact that $\bar{c}_2 = 0$ implies that as ϵ tends to zero, the diffusion-driven flow only distorts the contour line of the stratified scalar without amplifying the dispersion of the stratified scalar in the longitudinal direction of the channel.

So far, we have observed that the results obtained from the thin film approximation are consistent with the results obtained in § 3 when the density gradient vanishes, i.e. $\partial_{y_1}\bar{\rho} \to 0$, or equivalently when $\gamma \to 0$. Therefore, the thin film approximation presented here may not accurately model systems where the diffusion-driven flow significantly enhances dispersion, as is the case with the parameters provided in (3.25a–b), where the corresponding $\gamma = 9$–15 and the flow make visible enhancement of the scalar dispersion as shown in figure 10. For those parameter combinations, an asymptotic analysis using a scaling relation that differs from the one presented in this section become necessary.

6. Conclusion and discussion

This paper explores the diffusion-driven flow in a tilted parallel-plate channel domain with a nonlinear density stratification. By employing a novel asymptotic expansion provided in (3.3), we derive leading-order approximations for the velocity field (3.11) and (3.19), stratified scalar (3.11) and pressure field (3.21). Furthermore, we formulate an effective equation (3.16) to describe the cross-sectional averaged stratified scalar, and its accuracy is confirmed through numerical simulations of the governing equation (3.2).

The effective equation reveals that the dynamics of the stratified scalar depend on the dimensionless parameter γ, defined as $\gamma = (1/\sqrt{2})(-Re\,Pe\,Ri\sin\theta\partial_{y_1}\rho(\bar{c}))^{1/4} = (1/\sqrt{2})((gL^3\rho_0/\kappa\mu)\sin\theta\partial_{y_1}\rho(\bar{c}))^{1/4}$. When γ is large, the system behaves akin to a

diffusion equation with an enhanced diffusion coefficient of $1 + \cot^2 \theta$, where θ is the inclination angle relative to the horizontal plane. This result reveals an upper bound for the mixing capability of the diffusion-driven flow. Conversely, in the small γ limit, the behaviour of the stratified scalar approximates a pure diffusion process, with the diffusion-driven flow failing to amplify the dispersion of the stratified scalar significantly. Additionally, we demonstrate that in a confined domain with no-flux boundary conditions, the density profile in a system featuring diffusion-driven flow asymptotically converges to the one without flow over long times, although this convergence occurs on a time scale much larger than the diffusion time scale.

Moreover, we establish that the thin film approximation aligns with the results obtained using the novel expansion when the diffusion-driven flow is weak. In such scenarios, the stratified scalar can be modelled by a diffusion equation featuring molecular diffusivity, and the diffusion-driven flow primarily distorts the scalar distribution without significantly increasing longitudinal dispersion. Consequently, the thin film approximation falls short in describing systems with relatively large density gradients, where diffusion-driven flow markedly enhances dispersion. Importantly, we both numerically and theoretically demonstrate that the proposed expansion effectively addresses these situations.

Future research directions encompass several avenues. First, the passive scalar transport in the channel with non-flat boundaries has various practical applications (Chang & Santiago 2023; Roggeveen, Stone & Kurzthaler 2023). Therefore, our aim is to develop a reduced model of diffusion-driven flow in channels with rough boundaries, such as rock fissures or microfluidic devices. When the amplitude and wavelength of the boundary variation are small, the rough boundary with a no-slip boundary condition can be approximated by a flat wall with an effective slip boundary condition obtained through the multiscale method (Achdou, Pironneau & Valentin 1998; Carney & Engquist 2022). In this scenario, the method presented in our work can be readily applied. Alternatively, when the wavelength of the boundary variation is large, the asymptotic expansion presented by Mercer & Roberts (1990) could offer a solution. Second, while this work primarily focuses on analysing parallel plate domains, it is worth noting that the method proposed herein is applicable to channels with arbitrary cross-sections. Concentrating on the parallel plates domain stems from the availability of an exact solution for the auxiliary problem. Investigating this fundamental geometry can augment our understanding of domains with more complex shapes, such as tilted cylindrical cavities embedded in rocks (Sánchez, Higuera & Medina 2005), or tilted square containers (Page 2011*a*,*b*; French 2017; Grayer *et al.* 2020).

Author ORCID.
Lingyun Ding https://orcid.org/0000-0002-4622-3694.

Appendix. Numerical method

In this section, we document the numerical method used for solving the Navier–Stokes equation (2.6) and the effective equation (3.16).

To solve the Navier–Stokes equation (2.6), we employ the projection algorithm. During each iteration, we explicitly evaluate the advection term, while treating the viscosity term

implicitly. This involves solving a Poisson equation while enforcing the no-slip boundary condition. Subsequently, we solve the pressure Poisson equation, wherein adjustments are made to the velocity field to ensure fulfilment of the incompressibility condition. A comprehensive outline of the numerical scheme can be found in Hecht *et al.* (2005). We employ a similar approach for the advection–diffusion equation. In each step, the advection term is explicitly computed, whereas the diffusion term is treated implicitly, necessitating the resolution of a Poisson equation with a no-flux boundary condition. The time-stepping scheme used in this algorithm results in first-order accuracy in time. The finite element method is used to discretize the system of equations, and we implement the algorithm using the software FreeFEM++ (Hecht 2012).

The computational domain is defined as $\{(y_1, y_3) \mid y_1 \in [-5, 5], y_3 \in [0, 1]\}$. This domain is discretized using a triangular mesh with nearly uniform mesh sizes across the entire domain. In a typical simulation, the mesh consists of 17 594 vertices and 34 286 triangles. The simulation employs P1 elements, which correspond to linear functions defined over the triangles.

To simulate the effective equation (3.16) for comparison with the simulation of the governing equation (2.6), we employ the Fourier spectral method, as detailed in the work by Ding & McLaughlin (2022*a*), which incorporates a third-order implicit–explicit Runge–Kutta scheme proposed in Pareschi & Russo (2005). Specifically, we utilize the explicit Runge–Kutta method for integrating the nonlinear terms, while the diffusion term is handled using the implicit Runge–Kutta method. To ensure a meaningful comparison between our simulations and those based on the complete governing equations, we specify our computational domain as $y_1 \in [-5, 5]$. Additionally, we enforce no-flux boundary conditions at the endpoints of this interval to guarantee the conservation of mass. The Fourier spectral method is particularly effective for periodic domains, but we encounter no-flux boundary conditions in the y_1-direction. To overcome this problem, we implement an even extension, mirroring functions at $x = 5$, to establish periodic conditions on the extended domain $[-5, 15]$. The Fourier expansion of the even-extended function yields the cosine expansion of the original function. Each cosine function in the expansion has a zero derivative at the endpoints ($y_1 = \pm 5$), ensuring that the no-flux boundary condition is satisfied on the original domain $[-5, 5]$. The original domain comprises $2^{10} + 1$ grid points, while the extended domain encompasses 2^{11} grid points. The typical grid size is 0.0098, and the typical time step size is 9.7561×10^{-5}.

REFERENCES

ABAID, N., ADALSTEINSSON, D., AGYAPONG, A. & MCLAUGHLIN, R.M. 2004 An internal splash: levitation of falling spheres in stratified fluids. *Phys. Fluids* **16** (5), 1567–1580.

ACHDOU, Y., PIRONNEAU, O. & VALENTIN, F. 1998 Effective boundary conditions for laminar flows over periodic rough boundaries. *J. Comput. Phys.* **147** (1), 187–218.

ALLSHOUSE, M.R. 2010 Novel applications of diffusion-driven flow. PhD thesis, Massachusetts Institute of Technology.

ALLSHOUSE, M.R., BARAD, M.F. & PEACOCK, T. 2010 Propulsion generated by diffusion-driven flow. *Nat. Phys.* **6** (7), 516–519.

AREF, H., *et al.* 2017 Frontiers of chaotic advection. *Rev. Mod. Phys.* **89** (2), 025007.

ARIS, R. 1956 On the dispersion of a solute in a fluid flowing through a tube. *Proc. R. Soc. Lond.* A *Math. Phys. Sci.* **235** (1200), 67–77.

AULBACH, B. & WANNER, T. 1996 Integral manifolds for Carathéodory type differential equations in Banach spaces. In *Six Lectures on Dynamical Systems*, vol. 2. World Scientific.

AULBACH, B. & WANNER, T. 1999 Invariant foliations for Carathéodory type differential equations in Banach spaces. In *Advances of Stability Theory at the End of XX Century*. Gordon & Breach Publishers.

BALAKOTAIAH, V., CHANG, H.-C. & SMITH, F.T. 1995 Dispersion of chemical solutes in chromatographs and reactors. *Phil. Trans. R. Soc. Lond. Ser.* A *Phys. Engng Sci.* **351** (1695), 39–75.

BRAUNSFURTH, M.G., SKELDON, A.C., JUEL, A., MULLIN, T. & RILEY, D.S. 1997 Free convection in liquid gallium. *J. Fluid Mech.* **342**, 295–314.

CAMASSA, R., DING, L., MCLAUGHLIN, R.M., OVERMAN, R., PARKER, R. & VAIDYA, A. 2022 Critical density triplets for the arrestment of a sphere falling in a sharply stratified fluid. In *Recent Advances in Mechanics and Fluid-Structure Interaction with Applications: The Bong Jae Chung Memorial Volume*, p. 69. Springer.

CAMASSA, R., HARRIS, D.M., HUNT, R., KILIC, Z. & MCLAUGHLIN, R.M. 2019 A first-principle mechanism for particulate aggregation and self-assembly in stratified fluids. *Nat. Commun.* **10** (1), 1–8.

CARNEY, S.P. & ENGQUIST, B. 2022 Heterogeneous multiscale methods for rough-wall laminar viscous flow. *Commun. Math. Sci.* **20** (8), 2069–2106.

CARR, J. 1979 *Applications of Centre Manifold Theory*. Lefschetz Center for Dynamical Systems, Division of Applied Mathematics.

CENEDESE, C. & ADDUCE, C. 2008 Mixing in a density-driven current flowing down a slope in a rotating fluid. *J. Fluid Mech.* **604**, 369–388.

CHANG, R. & SANTIAGO, J.G. 2023 Taylor dispersion in arbitrarily shaped axisymmetric channels. *J. Fluid Mech.* **976**, A30.

CHASHECHKIN, Y.D. 2018 Waves, vortices and ligaments in fluid flows of different scales. *Phys. Astron. Intl J.* **2** (2), 105–108.

CHASHECHKIN, Y.D. & MITKIN, V.V. 2004 A visual study on flow pattern around the strip moving uniformly in a continuously stratified fluid. *J. Vis.* **7** (2), 127–134.

CHATWIN, P.C. 1970 The approach to normality of the concentration distribution of a solute in a solvent flowing along a straight pipe. *J. Fluid Mech.* **43** (2), 321–352.

DELL, R.W. & PRATT, L.J. 2015 Diffusive boundary layers over varying topography. *J. Fluid Mech.* **769**, 635–653.

DIMITRIEVA, N.F. 2019 Stratified flow structure near the horizontal wedge. *Fluid Dyn.* **54**, 940–947.

DING, L. 2022 Scalar transport and mixing. PhD thesis, The University of North Carolina at Chapel Hill.

DING, L. 2023 Shear dispersion of multispecies electrolyte solutions in the channel domain. *J. Fluid Mech.* **970**, A27.

DING, L., HUNT, R., MCLAUGHLIN, R.M. & WOODIE, H. 2021 Enhanced diffusivity and skewness of a diffusing tracer in the presence of an oscillating wall. *Res. Math. Sci.* **8** (3), 1–29.

DING, L. & MCLAUGHLIN, R.M. 2022*a* Determinism and invariant measures for diffusing passive scalars advected by unsteady random shear flows. *Phys. Rev. Fluids* **7** (7), 074502.

DING, L. & MCLAUGHLIN, R.M. 2022*b* Ergodicity and invariant measures for a diffusing passive scalar advected by a random channel shear flow and the connection between the Kraichnan-Majda model and Taylor-Aris dispersion. *Phys.* D*: Nonlinear Phenom.* **432**, 133118.

DING, L. & MCLAUGHLIN, R.M. 2023 Dispersion induced by unsteady diffusion-driven flow in a parallel-plate channel. *Phys. Rev. Fluids* **8**, 084501.

DRAKE, H.F., FERRARI, R. & CALLIES, J. 2020 Abyssal circulation driven by near-boundary mixing: water mass transformations and interior stratification. *J. Phys. Oceanogr.* **50** (8), 2203–2226.

FRENCH, A. 2017 Diffusion-driven flow in three dimensions. PhD thesis, Monash University.

GILL, W.N. 1967 A note on the solution of transient dispersion problems. *Proc. R. Soc. Lond.* A *Math. Phys. Sci.* **298** (1454), 335–339.

GRAYER, H., YALIM, J., WELFERT, B.D. & LOPEZ, J.M. 2020 Dynamics in a stably stratified tilted square cavity. *J. Fluid Mech.* **883**, A62.

GRAYER, H. II, YALIM, J., WELFERT, B.D. & LOPEZ, J.M. 2021 Stably stratified square cavity subjected to horizontal oscillations: responses to small amplitude forcing. *J. Fluid Mech.* **915**, A85.

HALL, R.E. 1924 The densities and specific volumes of sodium chloride solutions at 25°C. *J. Washington Acad. Sci.* **14** (8), 167–173.

HECHT, F. 2012 New development in Freefem++. *J. Numer. Maths* **20** (3–4), 251–266.

HECHT, F., PIRONNEAU, O., LE HYARIC, A. & OHTSUKA, K. 2005 *Freefem++ Manual*. Laboratoire Jacques Louis Lions.

HEITZ, R., PEACOCK, T. & STOCKER, R. 2005 Optimizing diffusion-driven flow in a fissure. *Phys. Fluids* **17** (12), 128104.

HOLMES, R.M., DE LAVERGNE, C. & MCDOUGALL, T.J. 2019 Tracer transport within abyssal mixing layers. *J. Phys. Oceanogr.* **49** (10), 2669–2695.

KISTOVICH, A.V. & CHASHECHKIN, Y.D. 1993 The structure of transient boundary flow along an inclined plane in a continuously stratified medium. *Z. Angew. Math. Mech.* **57** (4), 633–639.

KONDIC, L. 2003 Instabilities in gravity driven flow of thin fluid films. *SIAM Rev.* **45** (1), 95–115.

LEVITSKY, V.V., DIMITRIEVA, N.F. & CHASHECHKIN, Y.D. 2019 Visualization of the self-motion of a free wedge of neutral buoyancy in a tank filled with a continuously stratified fluid and calculation of perturbations of the fields of physical quantities putting the body in motion. *Fluid Dyn.* **54**, 948–957.

LIN, Z., THIFFEAULT, J.-L. & DOERING, C.R. 2011 Optimal stirring strategies for passive scalar mixing. *J. Fluid Mech.* **675**, 465–476.

LINDEN, P.F. 1979 Mixing in stratified fluids. *Geophys. Astrophys. Fluid Dyn.* **13** (1), 3–23.

LINDEN, P.F. & WEBER, J.E. 1977 The formation of layers in a double-diffusive system with a sloping boundary. *J. Fluid Mech.* **81** (4), 757–773.

MAGNAUDET, J. & MERCIER, M.J. 2020 Particles, drops, and bubbles moving across sharp interfaces and stratified layers. *Annu. Rev. Fluid Mech.* **52**, 61–91.

MERCER, G.N. & ROBERTS, A.J. 1990 A centre manifold description of contaminant dispersion in channels with varying flow properties. *SIAM J. Appl. Math.* **50** (6), 1547–1565.

MERCIER, M.J., ARDEKANI, A.M., ALLSHOUSE, M.R., DOYLE, B. & PEACOCK, T. 2014 Self-propulsion of immersed objects via natural convection. *Phys. Rev. Lett.* **112** (20), 204501.

MORE, R.V. & ARDEKANI, A.M. 2023 Motion in stratified fluids. *Annu. Rev. Fluid Mech.* **55**, 157–192.

NEWMAN, W.I. 1984 A Lyapunov functional for the evolution of solutions to the porous medium equation to self-similarity. I. *J. Math. Phys.* **25** (10), 3120–3123.

OERLEMANS, J. & GRISOGONO, B. 2002 Glacier winds and parameterisation of the related surface heat fluxes. *Tellus* A **54** (5), 440–452.

PAGE, M.A. 2011*a* Combined diffusion-driven and convective flow in a tilted square container. *Phys. Fluids* **23** (5), 056602.

PAGE, M.A. 2011*b* Steady diffusion-driven flow in a tilted square container. *Q. J. Mech. Appl. Maths* **64** (3), 319–348.

PARESCHI, L. & RUSSO, G. 2005 Implicit–explicit Runge–Kutta schemes and applications to hyperbolic systems with relaxation. *J. Sci. Comput.* **25** (1), 129–155.

PAVLIOTIS, G. & STUART, A. 2008 *Multiscale Methods: Averaging and Homogenization*. Springer Science & Business Media.

PHILLIPS, O.M. 1970 On flows induced by diffusion in a stably stratified fluid. In *Deep Sea Research and Oceanographic Abstracts*, vol. 17, pp. 435–443. Elsevier.

POLYANIN, A.D. & ZAITSEV, V.F. 2012 *Handbook of Nonlinear Partial Differential Equations: Exact Solutions, Methods, and Problems*. Chapman and Hall/CRC.

PRANDTL, L., OSWATITSCH, K. & WIEGHARDT, K. 1942 *Führer durch die strömungslehre (Essentials of Fluid Mechanics)*, pp. 105–108. Fried. Vieweg & Sohn.

ROBERTS, A.J. 1988 The application of centre-manifold theory to the evolution of system which vary slowly in space. *ANZIAM J.* **29** (4), 480–500.

ROBERTS, A.J. 1996 Low-dimensional models of thin film fluid dynamics. *Phys. Lett.* A **212** (1-2), 63–71.

ROBERTS, A.J. 2014 *Model Emergent Dynamics in Complex Systems*, vol. 20. SIAM.

ROBERTS, A.J. 2015 Macroscale, slowly varying, models emerge from the microscale dynamics. *IMA J. Appl. Maths* **80** (5), 1492–1518.

ROBERTS, A.J. & LI, Z. 2006 An accurate and comprehensive model of thin fluid flows with inertia on curved substrates. *J. Fluid Mech.* **553**, 33–73.

ROGGEVEEN, J.V., STONE, H.A. & KURZTHALER, C. 2023 Transport of a passive scalar in wide channels with surface topography: an asymptotic theory. *J. Phys.: Condens. Matter* **35** (27), 274003.

SÁNCHEZ, F., HIGUERA, F.J. & MEDINA, A. 2005 Natural convection in tilted cylindrical cavities embedded in rocks. *Phys. Rev.* E **71** (6), 066308.

SHAUGHNESSY, E.J. & VAN GILDER, J.W. 1995 Low rayleigh number conjugate convection in straight inclined fractures in rock. *Numer. Heat Transfer* A: *Appl.* **28** (4), 389–408.

SMITH, R. 1982 Contaminant dispersion in oscillatory flows. *J. Fluid Mech.* **114**, 379–398.

TAYLOR, G.I. 1953 Dispersion of soluble matter in solvent flowing slowly through a tube. *Proc. R. Soc. Lond.* A *Math. Phys. Sci.* **219** (1137), 186–203.

THIFFEAULT, J.-L. 2012 Using multiscale norms to quantify mixing and transport. *Nonlinearity* **25** (2), R1.

THOMAS, J. & CAMASSA, R. 2023 Self-induced flow over a cylinder in a stratified fluid. *J. Fluid Mech.* **964**, A38.

VAN DYKE, M. 1987 Slow variations in continuum mechanics. *Adv. Appl. Mech.* **25**, 1–45.

VITAGLIANO, V. & LYONS, P.A. 1956 Diffusion coefficients for aqueous solutions of sodium chloride and barium chloride. *J. Am. Chem. Soc.* **78** (8), 1549–1552.

WOODS, A.W. & LINZ, S.J. 1992 Natural convection and dispersion in a tilted fracture. *J. Fluid Mech.* **241**, 59–74.

WU, Z. & CHEN, G.Q. 2014 Approach to transverse uniformity of concentration distribution of a solute in a solvent flowing along a straight pipe. *J. Fluid Mech.* **740**, 196–213.

WUNSCH, C. 1970 On oceanic boundary mixing. In *Deep Sea Research and Oceanographic Abstracts*, vol. 17, pp. 293–301. Elsevier.

YOUNG, W.R. & JONES, S. 1991 Shear dispersion. *Phys. Fluids* A*: Fluid Dyn.* **3** (5), 1087–1101.

ZAGUMENNYI, I.V. & DIMITRIEVA, N.F. 2016 Diffusion induced flow on a wedge-shaped obstacle. *Phys. Scr.* **91** (8), 084002.